NEUROSCIENCE

Astrocytic GLUT1 reduction paradoxically improves central and peripheral glucose homeostasis

Carlos G. Ardanaz[1,2], Aida de la Cruz[3], Paras S. Minhas[4], Nira Hernández-Martín[5,6], Miguel Ángel Pozo[5,7,8], M. Pilar Valdecantos[9,10,11], Ángela M. Valverde[9,10], Palmira Villa-Valverde[12], Marcos Elizalde-Horcada[13], Elena Puerta[1,2], María J. Ramírez[1,2], Jorge E. Ortega[14,15,16], Ainhoa Urbiola[2,17], Cristina Ederra[2,17], Mikel Ariz[2,17,18], Carlos Ortiz-de-Solórzano[2,17], Joaquín Fernández-Irigoyen[19], Enrique Santamaría[20], Gerard Karsenty[21], Jens C. Brüning[22,23,24,25], Maite Solas[1,2]*

Astrocytes are considered an essential source of blood-borne glucose or its metabolites to neurons. Nonetheless, the necessity of the main astrocyte glucose transporter, i.e., GLUT1, for brain glucose metabolism has not been defined. Unexpectedly, we found that brain glucose metabolism was paradoxically augmented in mice with astrocytic GLUT1 reduction (GLUT1$^{\Delta GFAP}$ mice). These mice also exhibited improved peripheral glucose metabolism especially in obesity, rendering them metabolically healthier. Mechanistically, we observed that GLUT1-deficient astrocytes exhibited increased insulin receptor–dependent ATP release, and that both astrocyte insulin signaling and brain purinergic signaling are essential for improved brain function and systemic glucose metabolism. Collectively, we demonstrate that astrocytic GLUT1 is central to the regulation of brain energetics, yet its depletion triggers a reprogramming of brain metabolism sufficient to sustain energy requirements, peripheral glucose homeostasis, and cognitive function.

INTRODUCTION

The precise coupling between energy production and energy demand is still an important conundrum regarding brain metabolism. The brain is one of the most energy-demanding organs in the body and shows an urgent reliance on glucose. Despite representing only 2% of the body weight, the human brain accounts for approximately 25% of the total resting body glucose consumption (*1*, *2*). Arterial blood-borne glucose is the obligatory and major energy source for the brain (*3*). Alternative substrates can also be metabolized by the brain, but none of them can fully replace glucose (*4*). Brain glucose supply is critical for memory acquisition and consolidation at the hippocampal level (*5*, *6*). Besides, central nervous system (CNS) glucose availability is also sensed by specialized hypothalamic circuits that monitor the body energy state and regulate systemic glucose metabolism accordingly (*7*, *8*). This suggests that central energy metabolism is intimately linked not only to local brain activity but also to peripheral metabolism.

Brain glucose supply is controlled by glucose transporters (GLUTs). Specifically, to reach brain cells, blood glucose is transported across endothelial membranes via GLUT1. Endothelial cells are ensheathed by the endfeet of astrocytes, whose major GLUT is also GLUT1 (*9*, *10*). Thus, astrocytes are located in a privileged position to control the access of glucose into the brain (*11*). Although glucose can be delivered directly to neurons, which express GLUT3 and GLUT4 (*12*, *13*), one of the most popular theories explaining brain glucose dynamics is the astrocyte-neuron lactate shuttle (ANLS) (*14*). The ANLS model postulates that neuronal activity increases astrocytic glucose uptake and glycolysis, producing lactate. This lactate is subsequently exported to the extracellular space and imported by neurons via monocarboxylate transporters (MCTs). Once in neurons, lactate is oxidized to produce adenosine 5′-triphosphate (ATP). The ANLS hypothesis is supported by multiple studies, demonstrating a lactate gradient from astrocytes to neurons in vivo (*15*) or the astrocytic release of lactate upon arousal-induced cortical activity (*16*). However, the ANLS theory has faced a long-term controversy (*17*, *18*), as evidence has arisen that neuronal activation prompts neuronal glucose consumption without lactate uptake (*19*, *20*), active synapses require glucose consumption to maintain neurotransmitter vesicle recycling

---

[1] Department of Pharmaceutical Sciences, Division of Pharmacology, University of Navarra, 31008 Pamplona, Spain. [2] IdiSNA, Navarra Institute for Health Research, 31008 Pamplona, Spain. [3] Laboratory of Local Translation in Neurons and Glia, Achucarro Basque Centre for Neuroscience, 48940 Leioa, Spain. [4] Department of Medicine, Memorial Sloan Kettering Cancer Center, New York, NY, USA. [5] Unidad de Cartografía Cerebral, Instituto Pluridisciplinar, Universidad Complutense de Madrid, 28040 Madrid, Spain. [6] PET Center, Department of Radiology and Biomedical Imaging, Yale School of Medicine, New Haven, CT, USA. [7] Unidad de Cartografía Cerebral, Instituto de Investigación Sanitaria, Hospital Clínico San Carlos (IdISSC), 28040 Madrid, Spain. [8] Departamento de Fisiología, Facultad de Medicina, Universidad Complutense de Madrid, 28040 Madrid, Spain. [9] Instituto de Investigaciones Biomédicas Sols-Morreale, CSIC-UAM, Department of Metabolism and Cellular Signaling, Madrid 28029, Spain. [10] Centro de Investigación Biomédica en Red de Diabetes y Enfermedades Metabólicas Asociadas (CIBERDEM), ISCIII, Madrid 28029, Spain. [11] Universidad Francisco de Vitoria, Faculty of Experimental Sciences, Pozuelo de Alarcon, Madrid, Spain. [12] ICTS Bioimagen Complutense, Universidad Complutense de Madrid, Madrid, Spain. [13] Institut d'Investigació Sanitaria Pere Virgili (IISPV), 43204 Reus, Spain. [14] Centro de Investigación Biomédica en Red de Salud Mental (CIBERSAM), Spain. [15] Department of Pharmacology, University of the Basque Country (UPV/EHU), 48940 Leioa, Spain. [16] Biobizkaia Health Research Institute, 48903 Barakaldo, Spain. [17] Imaging Platform, Foundation for Applied Medical Research (FIMA), University of Navarra (UNAV), 31008 Pamplona, Spain. [18] Department of Electrical, Electronic and Communications Engineering, Public University of Navarra, 31006 Pamplona, Spain. [19] Proteomics Platform, Navarrabiomed, Hospital Universitario de Navarra (HUN), Universidad Pública de Navarra (UPNA), IdiSNA, 31008 Pamplona, Spain. [20] Clinical Neuroproteomics Unit, Navarrabiomed, Hospital Universitario de Navarra (HUN), Universidad Pública de Navarra (UPNA), IdiSNA, 31008 Pamplona, Spain. [21] Department of Genetics and Development, Vagelos College of Physicians and Surgeons, Columbia University, 701 West 168th Street, New York, NY, USA. [22] Max Planck Institute for Metabolism Research, Department of Neuronal Control of Metabolism, 50931 Cologne, Germany. [23] Center for Endocrinology, Diabetes and Preventive Medicine (CEDP), University Hospital Cologne, 50924 Cologne, Germany. [24] Excellence Cluster on Cellular Stress Responses in Aging Associated Diseases (CECAD) and Center of Molecular Medicine Cologne (CMMC), University of Cologne, 50931 Cologne, Germany. [25] National Center for Diabetes Research (DZD), 85764 Neuherberg, Germany.
*Corresponding author. Email: msolaszu@unav.es

and efficient synaptic transmission (*12*, *21*), and brain rhythms featuring high energy expenditure are only fully sustained by glucose and not lactate (*21*, *22*).

Recent mounting evidence shows that, although traditionally considered as mainly glycolytic, astrocytes can adapt their metabolism depending on the nature of the available fuel. It is therefore increasingly accepted that these glial cells can be metabolically adaptable, allowing them to switch between consuming different substrates (*23*–*25*). Despite the progressive acceptance of this newly adopted "astrocytic resilience" idea within the principles underlying brain energetics, the question of whether brain glucose metabolism can be sustained in the absence of astrocytic glucose transport remains unexplored. Although astrocytes are highly glycolytic and play a key role in the central regulation of energy homeostasis (*25*–*29*) and learning (*30*–*33*), the necessity of GLUT1, i.e., the main astrocytic GLUT, for the astrocytic contribution to these processes has never been studied. Here, we aimed to tackle these questions by generating a mouse model lacking GLUT1 specifically in astrocytes and assessing its abilities regarding systemic energy homeostasis and cognition, as well as the molecular and cellular features underlying these competences.

RESULTS

GLUT1 is necessary for glucose uptake and metabolism in astrocytes

To elucidate the contribution of GLUT1 to astrocytic glucose uptake and cellular metabolism, we cultured primary astrocytes from *Slc2a1*$^{\text{flox/flox}}$ mice and induced GLUT1 depletion via transfection with a Cre-expressing plasmid [GLUT1 knockdown (KD) cells]. Successful depletion of GLUT1 in astrocytes was confirmed by reductions of both *Slc2a1* mRNA expressions (Fig. 1A) and GLUT1 protein levels (Fig. 1, B and C) that resulted in a marked reduction of glucose uptake (Fig. 1D). Coherently, GLUT1 KD astrocytes exhibited lower extracellular lactate concentration over 7 days (Fig. 1E) and a diminished lactate release upon stimulation with glucose after starvation (Fig. 1F). Furthermore, real-time extracellular flux analysis revealed that GLUT1 KD astrocytes exhibited reduced glycolytic rate (Fig. 1, G to I). In view of this glycolytic deficiency, we assessed mitochondrial respiration, finding that GLUT1 KD astrocytes showed intact basal respiration but failed to reach the same degree of maximal respiration exhibited by control astrocytes (Fig. 1, J and K). Noteworthy, GLUT1 KD astrocytes were able to maintain a total ATP production rate comparable to that of control astrocytes (Fig. 1L). Thus, we hypothesized that in basal conditions, GLUT1 KD astrocytes are able to meet cellular energy demands using fuels other than glucose. GLUT1 KD astrocytes exhibited increased glutamine dependency (Fig. 1M) paired with largely unaltered fatty acid dependency (Fig. 1N). This higher reliance on glutamine oxidation was further corroborated by experiments indicating enhanced glutamine oxidation capacity (Fig. 1O). Overall, these results indicate that GLUT1 is fundamental for astrocytic glucose uptake and metabolism but not to maintain total ATP production.

GLUT1 reduction alters astrocytic reactivity and morphology

Given the essential contribution of GLUT1 to astrocytic metabolism shown above, we examined the effects of astrocytic GLUT1 KD within the mammalian brain (Fig. 2A). To demonstrate that astrocytes underwent Cre recombination subsequently resulting in a drop in GLUT1 levels, we purified astrocyte cell surface antigen-2 (ACSA-2$^+$) cells from the brains of adult mice (fig. S1A) and confirmed that *Slc2a1* mRNA expression (Fig. 2B) and GLUT1 protein levels (Fig. 2, C and D) were significantly decreased in ACSA-2$^+$ cells of GLUT1$^{\Delta\text{GFAP}}$ mice. In this scenario, it is tempting to postulate a potential compensation for the loss of GLUT1 by increased expression of other *Slc2a* members. Contrarily, the other members of the GLUT gene family showed unaltered mRNA expression in purified astrocytes upon GLUT1 decline, as well as a very low mRNA expression compared to that of *Slc2a1* (fig. S1B).

Astrocytes undergo a pronounced phenotypic transformation after brain injury and/or disease. To evaluate whether such a phenotype shift could be also occurring after GLUT1 depletion, we assessed their gene expression profile and morphology. The gene expression analyses showed that GLUT1$^{\Delta\text{GFAP}}$ astrocytes adopt a distinct molecular state, suggesting higher astrocytic reactivity (fig. S1C). This genetic signature modification was further accompanied by clear morphological alterations (Fig. 2E). GLUT1$^{\Delta\text{GFAP}}$ astrocytes display increased total process length (Fig. 2F), increased number of processes (Fig. 2G), and process thickness (Fig. 2H). However, despite the increased process arbor complexity, indicated by the large number of intersections in GLUT1$^{\Delta\text{GFAP}}$ astrocytes at the same radius (Fig. 2I), the Sholl analysis pointed out that enhanced complexity occurs at the same distance from the soma in GLUT1$^{\Delta\text{GFAP}}$ astrocytes (Fig. 2I). Together, these data indicate that GLUT1 KD triggers an increase of astrocytic process ramification but not elongation.

Astrocyte-specific GLUT1 depletion enhances brain glucose utilization notwithstanding a lower astrocytic glucose uptake

Despite the privileged position of astrocytes to control glucose access into the brain, whether astrocytic GLUT1 is fundamental for brain glucose metabolism in vivo remains unknown. To address this question, we subjected GLUT1$^{\Delta\text{GFAP}}$ and control mice to ^{18}F-fluorodeoxyglucose positron emission tomography (^{18}F-FDG–PET) scanning. Notably, GLUT1$^{\Delta\text{GFAP}}$ mice brains exhibited an enhanced ^{18}F-FDG–PET signal, not only at the whole-brain level (Fig. 3, A and B) but also in all individually analyzed brain regions (Fig. 3C). In light of this unexpected observation, we assessed whether this phenomenon was paired with increased brain glucose levels. To this end, we examined cerebrospinal fluid (CSF) glucose levels 30 min after intraperitoneal injection of glucose (2 g/kg) or vehicle (2 g/kg; saline), failing to find any differences in CSF glucose levels between GLUT1$^{\Delta\text{GFAP}}$ and control mice (Fig. 3D).

To elucidate brain glucose kinetics upon astrocytic GLUT1 reduction in a deeper manner, we performed dynamic PET (dPET) studies. While static PET provides a simple snapshot of radiopharmaceutical concentration, dPET with tracer kinetic modeling reveals the temporal dynamics of radiopharmaceutical incorporation and metabolism. dPET analysis showed that during the incorporation period (first 20 min), GLUT1$^{\Delta\text{GFAP}}$ mice showed improved glucose kinetics (fig. S2, A to D) which were maintained along the time, showing a significantly higher ^{18}F-FDG flux (ki) during the entire scan period (60 min; fig. S2E).

PET scans do not offer cellular resolution. Thus, one of the central questions that arises in this scenario is the identity of the cell type responsible for the enhanced glucose metabolism that occurs in GLUT1$^{\Delta\text{GFAP}}$ brains. Although the decreased 2-deoxyglucose-6-phosphate (2-DG6P)

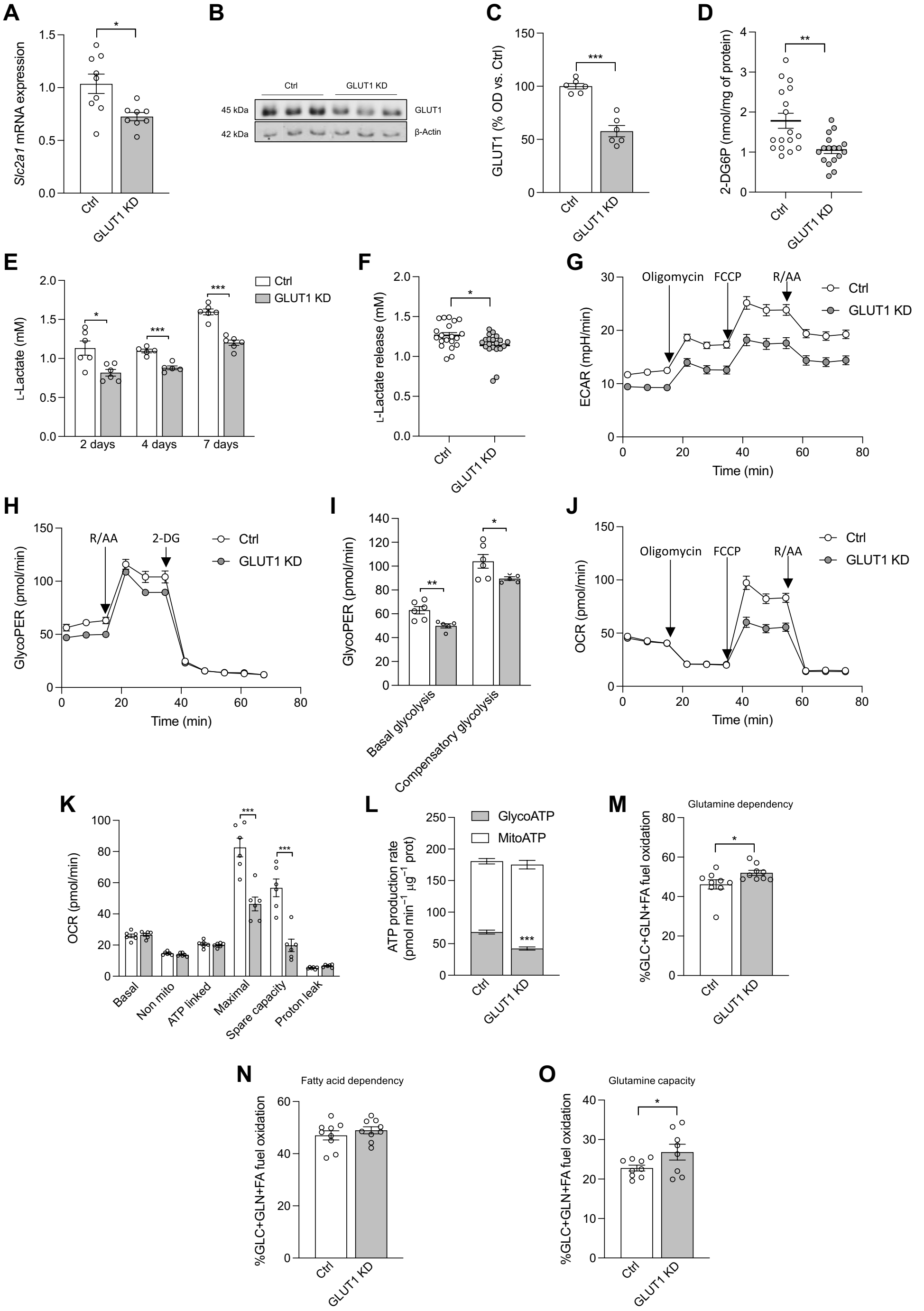

Fig. 1. GLUT1 is fundamental for astrocytic glucose uptake and metabolism but not to maintain total ATP production. (**A**) *Slc2a1* mRNA expression levels in primary cultured astrocytes without [control (Ctrl)] or with (GLUT1 KD) Cre recombination ($n = 8$ to 9 independently isolated astrocyte cultures). (**B**) GLUT1 protein expression level representative Western blot image and (**C**) quantification [optical density (OD)] in primary cultured astrocytes in Ctrl and GLUT1 KD cells ($n = 6$ independently isolated astrocyte cultures). (**D**) Glucose uptake in Ctrl and GLUT1 KD cultured astrocytes ($n = 17$ independent wells). (**E**) L-Lactate release in culture medium in Ctrl (Ctrl) and GLUT1 KD cultured astrocytes (in mM; $n = 6$ independently isolated astrocyte cultures). (**F**) L-Lactate release in culture medium after glucose starvation and subsequent glucose stimulation (in mM; $n = 20$ independent wells). (**G**) Glycolytic flux assessed by extracellular acidification rate (ECAR) in Ctrl and GLUT1 KD cultured astrocytes ($n = 9$ independent wells). FCCP, carbonyl cyanide-4 (trifluoromethoxy) phenylhydrazone; R, rotenone; AA, antimycin A. (**H**) Glycolysis-derived proton efflux rate (GlycoPER) assessment and (**I**) quantification of basal and compensatory glycolysis in Ctrl and GLUT1 KD cultured astrocytes ($n = 6$ independent wells). 2-DG, 2-deoxiglucose. (**J**) Mitochondrial respiration evaluation by oxygen consumption rate (OCR) and (**K**) quantification of mitochondrial respiration evaluation in Ctrl and GLUT1 KD cultured astrocytes ($n = 9$ independent wells). (**L**) Glycolysis- and mitochondrial respiration–derived ATP production rate in Ctrl and GLUT1 KD cultured astrocytes ($n = 9$ independent wells). (**M**) Glutamine dependency and (**N**) fatty acid dependency assay ($n = 9$ independent wells). (**O**) Glutamine oxidative capacity assessment ($n = 9$ independent wells). Data are presented as means ± SEM. $^{*}P \leq 0.05$, $^{**}P \leq 0.01$, and $^{***}P < 0.001$, as determined by two-tailed Student's *t* test in all cases.

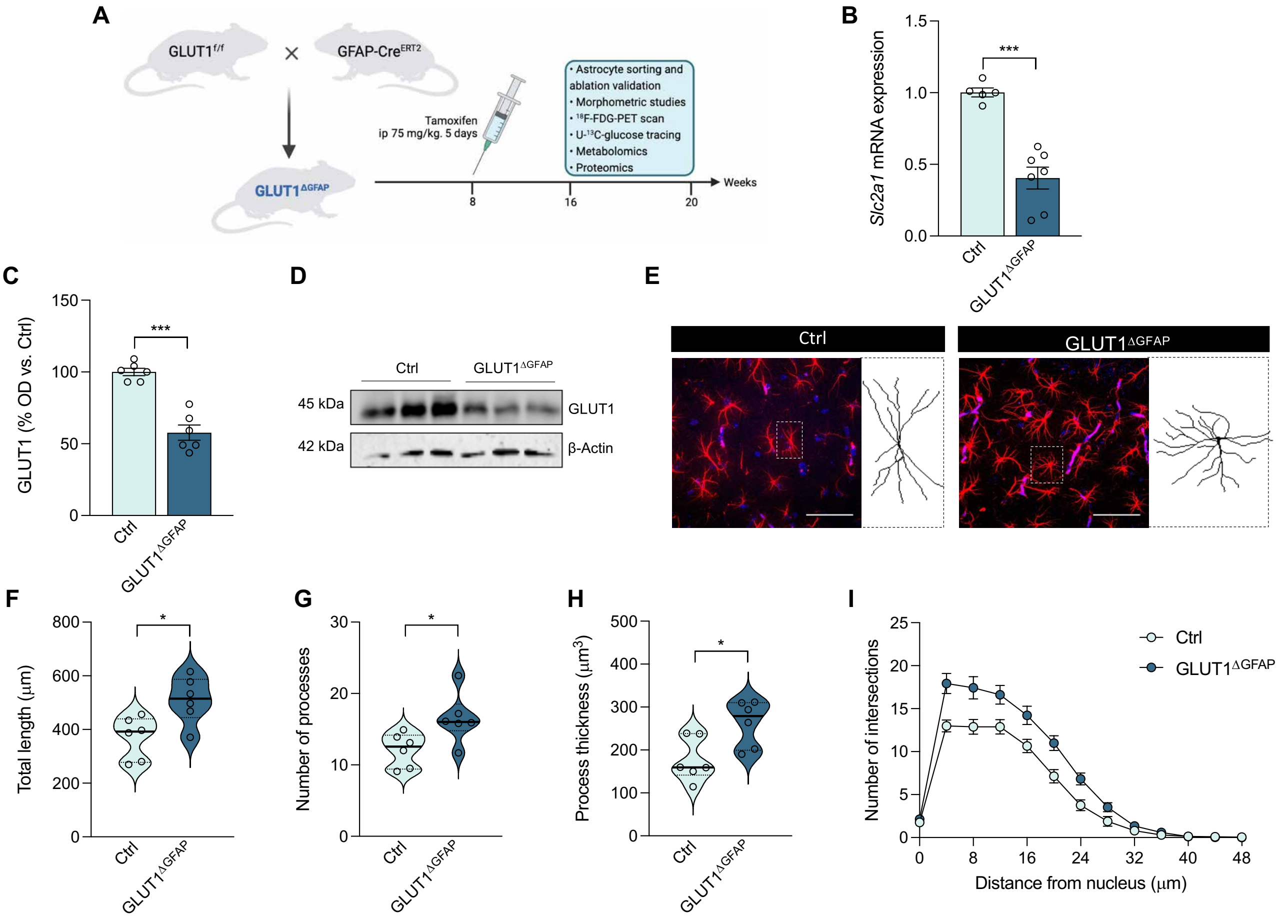

Fig. 2. Inducible in vivo depletion of astrocytic GLUT1 modifies astrocyte morphology. (**A**) Strategy used to generate mice lacking GLUT1 transporter specifically in astrocytes (GLUT1$^{\Delta GFAP}$) and their Ctrl littermates (GLUT1$^{f/f}$). Created with BioRender.com. (**B**) GLUT1 mRNA levels, (**C**) protein expression level quantification (OD), and (**D**) representative Western blotting image in Ctrl and GLUT1$^{\Delta GFAP}$ mice after ACSA-2^{+} fluorescence-activated cell sorting (FACS)–mediated separation of astrocytes ($n = 5$ to 6 mice per group). (**E**) Representative glial fibrillary acidic protein (GFAP; red)–4′,6-diamidino-2-phenylindole (DAPI; blue) cell micrograph and its respective reconstruction obtained from stratum radiatum astrocytes of Ctrl and GLUT1$^{\Delta GFAP}$ mice (representative image of $n = 6$ per group). Scale bar, 50 μm. (**F**) Quantification of the processes' total length, (**G**) number of processes, (**H**) GFAP process volume, and (**I**) Sholl analysis representing the astrocyte complexity ($n = 6$ animals per group and 10 astrocytes per animal). Data are presented as means ± SEM. $^{*}P \leq 0.05$ and $^{***}P \leq 0.001$, as determined by two-tailed Student's *t* test. ip, intraperitoneal.

uptake observed in cell culture (Fig. 1D) and the lack of GLUT compensation observed in fig. S1B suggests that GLUT1-depleted astrocytes could not show an improved glucose metabolism, we decided to question whether astrocytic glucose uptake in vivo is altered upon GLUT1 decrease. In an attempt to test this hypothesis, we decided to perform a cell-specific readout of metabolic fluxes in GLUT1$^{\Delta GFAP}$ mice. To this end, we infused [U-^{13}C]glucose to control and GLUT1$^{\Delta GFAP}$ mice for 3 hours via the femoral vein, isolated astrocytes 2 hours later, and measured labeled metabolites from the glycolytic pathway (Fig. 3E). KD of GLUT1 in astrocytes reduced the in vivo astrocytic incorporation of ^{13}C-glucose (Fig. 3F) and decreased the incorporation of ^{13}C-glucose into glycolytic cycle intermediates, consistent with decreased glucose flux within the astrocyte (fig. S2, F to I).

To further explore the metabolic change induced by the lower astrocytic glucose flux, we performed a metabolomics study in control and GLUT1$^{\Delta GFAP}$ mice. Hippocampus and hypothalamus (key areas for the present study) were analyzed. An unsupervised principal components analysis (PCA) was applied to the ^{1}H nuclear magnetic resonance (NMR) spectra of the control and GLUT1$^{\Delta GFAP}$ mice hippocampi or hypothalami, showing an absence of clustering patterns between samples. A supervised partial least squares discriminant analysis (PLS-DA) was then applied to identify a discriminatory metabolic pattern between both groups, finding a clear grouping along the scores, indicative of a radically different metabolic pattern between control and GLUT1$^{\Delta GFAP}$ mice hippocampi (Fig. 3G) and hypothalami (Fig. 3H). The resonances identified as significantly different by PCA loadings analysis were individually integrated for metabolic quantification. The most significantly changed metabolite appeared to be lactate, showing reduced levels in GLUT1$^{\Delta GFAP}$ brains compared to controls (Fig. 3I).

In an attempt to elucidate the global impact of the enhancement in glucose metabolism observed in GLUT1$^{\Delta GFAP}$ mice, we undertook a proteomic profiling of both control and GLUT1$^{\Delta GFAP}$ brains. We were able to identify 2329 proteins and performed weighted gene coexpression network analysis (WGCNA) identifying a total of 27 modules of proteins that were highly coexpressed

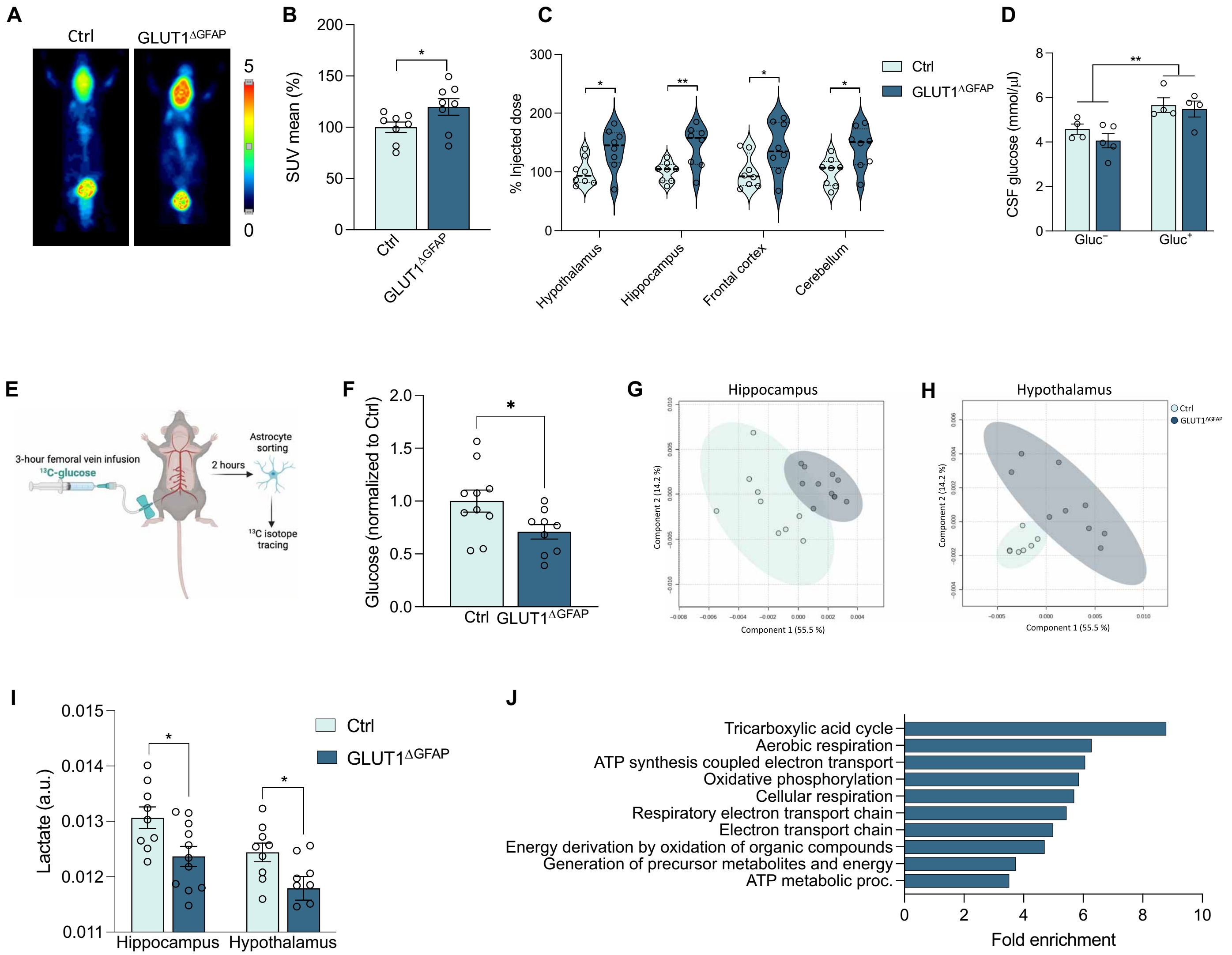

Fig. 3. Inducible in vivo depletion of astrocytic GLUT1 enhances CNS glucose utilization and shifts the whole energetic profile of the brain. (**A**) PET images of representative mice showing brain ^{18}F-FDG signal, (**B**) the quantification of positron emission [mean standardized uptake value (SUV)], and (**C**) ex vivo counting of radioactivity in dissected brain samples ($n = 8$ mice per group). (**D**) CSF glucose presence 30 min after intraperitoneal vehicle or glucose injection in Ctrl and GLUT1$^{\Delta GFAP}$ mice ($n = 4$ to 5 mice per group). (**E**) Schematic representation of U-^{13}C-glucose infusion and subsequent astrocyte sorting. Created with BioRender.com. (**F**) Quantification of U-^{13}C-glucose in sorted astrocytes ($n = 9$ to 10 mice per group). (**G**) Hippocampal and (**H**) hypothalamic PLS graphs of comparison between Ctrl and GLUT1$^{\Delta GFAP}$ mice. The graph shows the dispersion of the different individuals by genotype, where a clear grouping of the Ctrl group and GLUT1$^{\Delta GFAP}$ is seen, meaning differences in the metabolic profile of both groups ($n = 9$ mice per group). (**I**) Quantification of hippocampal and hypothalamic lactate levels in metabolomics studies ($n = 9$ mice per group). (**J**) Weighted gene coexpression network analysis (WGCNA) blue module gene ontology (GO) Biological Processes showing significant fold enrichment when comparing Ctrl and GLUT1$^{\Delta GFAP}$ mice ($n = 6$ per group). Data are presented as means ± SEM. $^{*}P \leq 0.05$ and $^{**}P \leq 0.01$, as determined by two-tailed Student's *t* test (B to D and F) and two-way analysis of variance (ANOVA) (I). a.u., arbitrary units.

across our cohorts of mice (fig. S3A). Only 1 of the 27 modules (termed "blue module") exhibited a high correlation with genotype (fig. S3, B to D). Crucially, gene ontology (GO) analysis of the blue module revealed that the first 10 GO Biological Processes showing significant fold enrichment were all related to cell energy metabolism (Fig. 3J). Considering that this proteomic profiling was not performed in purified astrocytes but in brain tissue containing all brain cell types, this result suggests that disrupting only astrocytic glucose metabolism is sufficient to shift the whole energetic profile of the brain.

Astrocytic GLUT1 depletion induces neither brain angioarchitecture alteration nor blood-brain barrier breakdown

Ablation of GLUT1 in blood-brain barrier (BBB) endothelial cells induces serious brain angioarchitecture and BBB integrity alterations (*34*). As astrocytic endfeet are an essential component of the BBB, we examined whether astrocytic GLUT1 KD could also induce such alterations. After demonstrating that the Cre/LoxP strategy used does not induce GLUT1 down-regulation in endothelial cells (fig. S4, A to C), our data revealed an absence of serum-borne proteins [immunoglobulin G (IgG) and fibrin] in capillary-depleted brains of GLUT1$^{\Delta GFAP}$ mice similar to that observed in control mice (fig. S4D). Besides, we could not find IgG (fig. S4E) or fibrin (fig. S4F) leaking out of vascular (lectin^{+}) areas, arguing against the possibility of BBB leakage in GLUT1$^{\Delta GFAP}$ mice. Consistently, the expression of the gap-junction proteins occludin (fig. S4, G, I and J) and zonulin-1 (ZO-1; fig. S4, H, I and J) was also unaltered, supporting the idea of an intact BBB integrity. Furthermore, we examined the brain microvascular structure by quantifying the length of vascular networks. Again, no significant changes were found between GLUT1$^{\Delta GFAP}$ and control mice (fig. S4K) in fractional vascular volume (fig. S4L) and/or vascular length (fig. S4M).

Systemic glucose homeostasis is improved upon astrocyte-specific GLUT1 depletion

To determine whether astrocytic GLUT1 is involved in maintaining whole-body glucose homeostasis, we investigated whether mice lacking GLUT1 in astrocytes display metabolic alterations. To this end, we performed experiments in mice fed with either a normal chow diet (NCD) or a high-fat diet (HFD) to account for how GLUT1$^{\Delta GFAP}$ mice cope with a metabolic challenge. Although no significant differences between genotypes were observed in either body weight (fig. S5A) or body composition (fig. S5B), we noted marked differences in feeding behavior. Specifically, GLUT1$^{\Delta GFAP}$ mice showed a greater ability to curb the fasting-elicited hyperphagic response (Fig. 4A), and they exhibited an increased suppression of hyperphagia in response to intraperitoneal glucose administration (Fig. 4B). Furthermore, HFD-fed GLUT1$^{\Delta GFAP}$ mice showed an enhanced capacity to readjust systemic glucose levels after intraperitoneal glucose injection–induced hyperglycemia (Fig. 4C) compared to HFD-fed control mice, without changes in systemic insulin sensitivity (fig. S5C). Nevertheless, the improved glucose tolerance in HFD-fed GLUT1$^{\Delta GFAP}$ mice was coupled with a pronounced increase in glucose-stimulated pancreatic insulin secretion (Fig. 4D). Thus, we analyzed the histological features of GLUT1$^{\Delta GFAP}$ mice pancreatic islets. We observed that HFD-fed GLUT1$^{\Delta GFAP}$ mice islets did not display the hyperplasic features typically shown by HFD-fed mice (Fig. 4E) but were indistinguishable from NCD-fed mice islets (fig. S5, D and E). This effect is not due to the possibility of a nonspecific GLUT1 targeting in the islet of Langerhans of the pancreas, as no glial fibrillary acidic protein (GFAP) expression was found in this tissue (fig. S5F).

The impact of astrocytic GLUT1 KD on the modulation of systemic energy metabolism was further substantiated when we assessed systemic substrate usage via indirect calorimetry in mice. Metabolism under astrocytic GLUT1 decrease shifts from a preferential carbohydrate usage to predominant fat utilization (Fig. 4F and fig. S5G), a phenomenon that is accompanied by a higher energy expenditure observed in GLUT1$^{\Delta GFAP}$ mice fed on a HFD (Fig. 4G and fig. S5H).

The above analyzed metabolic features are controlled by glucose-sensing proopiomelanocortin (POMC) neurons in the arcuate nucleus of the hypothalamus (ARC) (*35–38*). Noteworthy, it has been shown that astrocytes regulate POMC neuron activation (*25*, *39*). Hence, we evaluated the activity response of ARC POMC neurons using c-Fos immunoreactivity, uncovering that GLUT1$^{\Delta GFAP}$ mice displayed a markedly higher number of c-Fos^{+} POMC cells compared to control animals (Fig. 4, H and I). The increased POMC activity could be directly linked to the lower GFAP levels observed in the ARC of GLUT1$^{\Delta GFAP}$ mice, which results in a lower POMC coverage (Fig. 4J and fig. S5, I and J).

Brown adipose tissue (BAT) represents a core organ in control of glucose homeostasis. Hematoxylin and eosin (H&E) staining of BAT sections revealed that HFD-fed GLUT1$^{\Delta GFAP}$ mice did not present the typical obesity-related increased BAT adiposity, as observed in HFD-fed control mice, but displayed a morphology similar to that observed in NCD-fed mice (Fig. 4K). Considering that this phenotype could be correlated with a higher BAT activity, we examined the mRNA expression (Fig. 4L) and protein levels (fig. S5, K and L) of BAT uncoupling protein 1 (UCP1), finding that both were markedly up-regulated in GLUT1$^{\Delta GFAP}$ mice, especially when subjected to HFD feeding. Furthermore, we measured BAT activity by determining core body temperature during a cold exposure, finding that HFD-fed GLUT1$^{\Delta GFAP}$ mice were the most efficient group generating heat (Fig. 4M). All these results showing a higher BAT activity are intimately aligned with the higher energy expenditure exhibited by HFD-fed GLUT1$^{\Delta GFAP}$ mice (see Fig. 4G). It is known that glucose-mediated activation of locus coeruleus tyrosine hydroxylase (TH) neurons is necessary to increase BAT activity upon HFD feeding, preventing obesity (*40*). In our hands, the number of c-Fos^{+}–TH cells observed in GLUT1$^{\Delta GFAP}$ mice was, albeit nonsignificantly, increased (fig. S5, M and N), potentially contributing to the BAT phenotype and activity observed in those mice.

Considering that GFAP is also expressed in other tissues besides the CNS (*41*), we next investigated whether the reduction of GLUT1 specifically in ARC astrocytes is sufficient to elicit the beneficial effects observed in whole-brain GLUT1$^{\Delta GFAP}$ mice. To this end, we used adeno-associated virus (AAV)–mediated Cre recombination to delete GLUT1 specifically in GFAP^{+} astrocytes within the ARC (ARC-GLUT1$^{\Delta GFAP}$ mice). First, we confirmed that AAV delivery occurred specifically in the ARC and that Cre-expressing, AAV-infected cells were GFAP^{+}, i.e., astrocytes and not neurons (Fig. 4N and fig. S5O). ARC-specific astrocytic GLUT1 decrease elicited a phenotype that corresponded to that observed in whole-brain GLUT1$^{\Delta GFAP}$ mice, exhibiting a tendency toward decreased hyperphagia (fig. S5P) and improved glucose handling (Fig. 4O), paired with a markedly increased glucose-stimulated pancreatic insulin secretion (Fig. 4P) upon HFD. ARC-GLUT1$^{\Delta GFAP}$ did not recapitulate the BAT thermogenesis phenotype (fig. S5Q), indicating that astrocytic GLUT1 depletion in other areas, such as locus coeruleus, is required for this effect.

Astrocytic activation increases brain glucose metabolism in GLUT1$^{\Delta GFAP}$ mice

Given that brain glucose metabolism is strongly correlated with cognitive proficiency (*42*, *43*), we examined the ability of GLUT1$^{\Delta GFAP}$ mice to properly establish memory. After excluding locomotor activity alterations (fig. S6A), we tested recognition memory using the novel object recognition (NOR) task. Both NCD- and HFD-fed GLUT1$^{\Delta GFAP}$ mice were as competent as control mice at recognizing the familiar object (fig. S6B), with a slight improvement of GLUT1$^{\Delta GFAP}$ mice in the 24-hour task. We then compared the ability of the different groups of mice to adequately establish spatial memory in the Morris water maze (MWM) task. GLUT1$^{\Delta GFAP}$ mice were as efficient as control mice on spatial memory acquisition (fig. S6C) and memory retention (fig. S6D).

Given the slightly improved cognitive abilities upon astrocytic GLUT1 diminishment, we aimed to investigate its underlying histological correlates. First, we explored c-Fos immunoreactivity in the

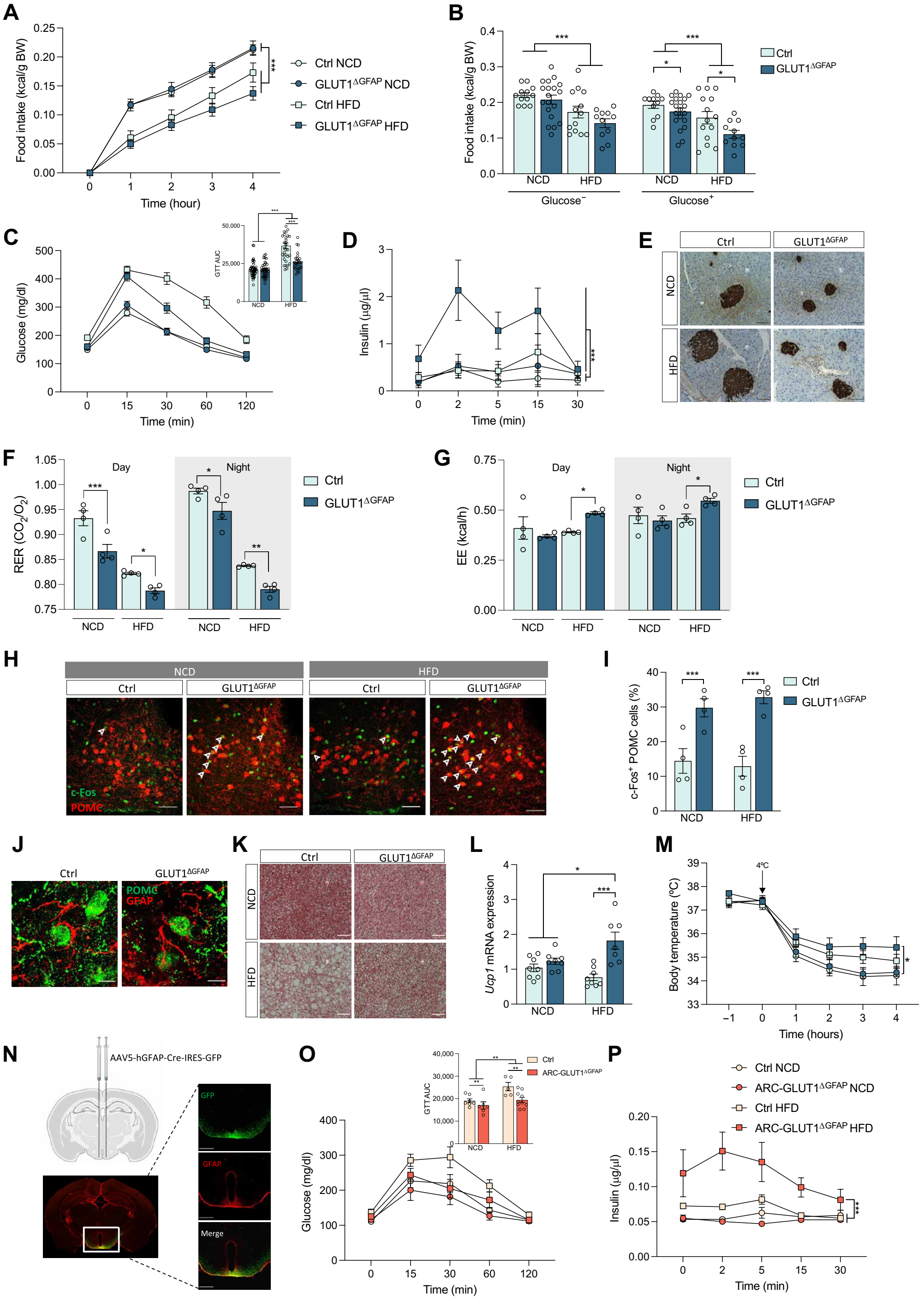

Fig. 4. Mice lacking GLUT1 in astrocytes exhibit improved glucose homeostasis. (**A**) Fasting-induced hyperphagic response and (**B**) 4-hour accumulated food intake after intraperitoneal injection of glucose ($n = 3$ to 21). (**C**) Glucose tolerance test (GTT) and the quantification of the area under the curve (AUC) and (**D**) glucose-stimulated insulin secretion [GSIS; $n = 25$ to 40 in (C); $n = 8$ in (D)]. (**E**) Representative pancreatic islet image ($n = 4$ and 10 islets per mouse). Scale bar, 100 µm. (**F**) Respiratory exchange rate (RER) and (**G**) energy expenditure ($n = 4$). Gray bars denote dark phases. (**H**) Representative c-Fos staining of POMC neurons of ARC and (**I**) quantification of c-Fos$^+$–POMC cells ($n = 4$ and 2 slices per mouse). Scale bar, 50 µm. (**J**) GFAP-labeled processes in contact with POMC neurons in the ARC of mice in HFD, 30 min after intraperitoneal glucose injection. Scale bar, 10 µm. (**K**) Hematoxylin and eosin (H&E) staining of brown adipose tissue ($n = 6$ and 2 slices per mouse). Scale bar, 100 µm. (**L**) *Ucp1* mRNA expression ($n = 8$). (**M**) Rectal temperature upon cold exposure (+4°C) for 4 hours ($n = 12$ to 20). (**N**) Representative illustration and immunostaining image depicting the area infected by adeno-associated virus 5 (AAV5)–hGFAP-Cre–internal ribosomal entry site (IRES)–green fluorescent protein (GFP) and GFAP immunoreactivity ($n = 7$ to 10). Scale bar, 500 µm. Created with BioRender.com. (**O**) GTT and quantification AUC and (**P**) GSIS in ARC-specific astrocytic GLUT1-ablated (ARC-GLUT1$^{\Delta GFAP}$) mice [$n = 5$ to 10 in (O); $n = 4$ in (P)]. Data are presented as means ± SEM. *$P \leq 0.05$, **$P \leq 0.01$, and ***$P \leq 0.001$, as determined by repeated-measurement ANOVA (A, C, D, M, O, and P) and two-way ANOVA followed by Tukey [(B and C) AUC and (F, G, I, L, and O) AUC].

dentate gyrus of the hippocampus, finding a markedly higher number of c-Fos$^+$ cells in GLUT1$^{\Delta GFAP}$ group compared to controls (Fig. 5, A and B). Accordingly, while Golgi-Cox staining revealed no differences between NCD-fed control and GLUT1$^{\Delta GFAP}$ mice hippocampal spine density, it evidenced that HFD-fed control mice had a slightly lower spine density, and this effect was reverted in HFD-fed GLUT1$^{\Delta GFAP}$ mice (Fig. 5, C and D).

As exposure to a cognitive-demanding training might affect brain glucose metabolism, we subjected all mice groups to ^{18}F-FDG–PET scanning immediately after the last MWM probe trial. Our data revealed increased ^{18}F-FDG brain signal in MWM-trained control mice compared to naïve control mice, and this enhancement was even larger in MWM-trained GLUT1$^{\Delta GFAP}$ mice (Fig. 5, E and F).

Learning and memory paradigms induce astrocytic activation (*44*). Therefore, we assessed whether an artificially induced astrocytic activation using chemogenetics could also cause an increase in brain glucose metabolism in GLUT1$^{\Delta GFAP}$ mice. To this end, we expressed the Gq-coupled human M3 muscarinic receptor (hM3Dq) in astrocytes of the CA1 area of the hippocampus, allowing for their activation by a designer drug [i.e., Clozapine-N-oxide (CNO)]. Noteworthy, astrocytic Gq-like activation induced a marked increase in glucose metabolism specifically in the hippocampus and not in other nonstimulated areas (Fig. 5, G and H). Considering that GLUT1 KD astrocytes show decreased glucose uptake (see Fig. 3F), other cells rather than astrocytes must be responsible for the increased brain glucose metabolism observed after GLUT1$^{\Delta GFAP}$ stimulation. On the basis of our data, it is tempting to speculate that the cell type responsible for the improved glucose metabolism could be neurons, as markedly higher c-Fos activity is observed in the hypothalamus (Fig. 4H) and the hippocampus (Fig. 5A) of GLUT1$^{\Delta GFAP}$ mice. This could imply that upon stimulation, GLUT1$^{\Delta GFAP}$ astrocytes communicate more efficiently with neighboring neurons than control astrocytes. Astrocytes can modulate neuronal activity through multiple mechanisms, with the release of gliotransmitters being the main one. Therefore, we decided to elucidate whether gliotransmitter release is induced when GLUT1 is depleted from astrocytes.

Brain purinergic signaling is essential for improved glucose homeostasis and memory preservation in astrocytic GLUT1-ablated mice

Several studies have shown that astrocytes can secrete a series of neurotransmitters, including glutamate, D-serine, and ATP, which are able to modulate the activity of nearby neurons (*45*–*48*). We studied the release of those gliotransmitters in GLUT1 KD astrocytic cell cultures, failing to find changes in serine (Fig. 6A) and glutamate (Fig. 6B) release to the cell media. ATP stands among the main bioactive molecules released by astrocytes (*49*), and according to our data, astrocytes maintain total ATP production rate despite GLUT1 depletion (Fig. 1L). This discovery led us to investigate whether GLUT1-ablated astrocytes also maintained their ability to release ATP. GLUT1 KD primary astrocytes featured increased ATP release to the extracellular medium (Fig. 6C) compared to control cells. Consistently, microdialysis-isolated interstitial fluid of freely moving GLUT1$^{\Delta GFAP}$ mice presented a larger increase in ATP concentration within the first 30 min after intraperitoneal glucose administration compared to control mice (Fig. 6D). To discard that this effect was not a consequence of the animal stress triggered by manipulation while injecting glucose, a cohort of mice were saline or glucose injected, demonstrating that saline administration did not induce any rise of ATP levels in the interstitial fluid (fig. S7A). Therefore, we hypothesized that enhanced brain purinergic signaling could be essential for the systemic glucose homeostasis improvement and memory preservation displayed by GLUT1$^{\Delta GFAP}$ mice. We found that acute intracerebroventricular administration of pyridoxalphosphate-6-azophenyl-2′,4′-disulfonic acid (PPADS; Fig. 6E), a nonselective P2 purinergic antagonist, totally abrogated both the improved glucose-induced suppression of feeding in NCD (fig. S7B) or HFD (Fig. 6F) and the enhanced glucose tolerance shown by vehicle-treated GLUT1$^{\Delta GFAP}$ mice [NCD (fig. S7C) and HFD (Fig. 6G)]. Moreover, PPADS-treated GLUT1$^{\Delta GFAP}$ mice exhibited worsened memory in both the NOR [NCD (fig. S7D) and HFD (Fig. 6H)] and MWM tasks particularly on HFD (Fig. 6, I to K; data in NCD: fig. S7, E and F). Together, these results demonstrate that brain-specific purinergic signaling is necessary for the improved peripheral metabolism and memory persistence phenotypes upon astrocyte-specific GLUT1 reduction.

Astrocytic insulin receptor mediates enhanced ATP release and its depletion impairs glucose homeostasis and memory

Astrocytic insulin signaling is essential for insulin-dependent ATP release by astrocytes (*48*). We found that fluorescence-activated cell sorting (FACS)–purified astrocytes from GLUT1$^{\Delta GFAP}$ mice brains exhibited increased insulin receptor (IR) expression (Fig. 7A). It is thus plausible that astrocyte IR overexpression upon GLUT1 decline mediates enhanced astrocytic insulin-stimulated ATP release. To test this hypothesis, we crossed *Insr*$^{flox/flox}$ (named IR$^{f/f}$) mice with hGFAP-CreER$^{T2+/-}$ to obtain the hGFAP-CreER$^{T2+/-}$:IR$^{f/f}$ (named IR$^{\Delta GFAP}$ group) line. Tamoxifen-induced IR depletion was confirmed in sorted astrocytes (fig. S8A). Crucially, IR$^{\Delta GFAP}$ mice failed to increase brain interstitial fluid ATP concentration triggered by intraperitoneal glucose administration (which prompts a physiological insulin release) to the same extent as GLUT1$^{\Delta GFAP}$ (Fig. 7B).

To further test the relevance of astrocytic IR for energy homeostasis and cognition, we studied glucose metabolism and memory formation in IR$^{\Delta GFAP}$ mice. In agreement with previous studies (*25*), we found that IR$^{\Delta GFAP}$ mice displayed reduced brain glucose utilization assessed by ^{18}F-FDG–PET (fig. S8, B to G) and decreased glucose concentration in the CSF (fig. S8H). Metabolically, although gaining the same body weight as control mice (fig. S8I), IR$^{\Delta GFAP}$ mice displayed reduced glucose-induced suppression of hyperphagia (fig. S8J) and lower glucose tolerance (fig. S8K) in the presence of unaltered insulin sensitivity (fig. S8L). Provided that brain insulin signaling has an important role in memory and learning (*6*, *50*, *51*) and that its disruption has been linked to cognitive dysfunction (*52*–*54*), we examined recognition and spatial memory in IR$^{\Delta GFAP}$ mice. Compared to control mice, although exhibiting identical locomotor activity (fig. S8M), IR$^{\Delta GFAP}$ mice were less efficient in memorizing objects in the NOR task (fig. S8N) and exhibited impaired spatial memory (fig. S8, O and P).

Given the necessity of astrocytic IR for glucose-stimulated increases of brain ATP concentrations demonstrated above (Fig. 7B), we hypothesized that insufficient brain purinergic signaling could be one of the causes underlying the aberrant metabolic and cognitive phenotypes presented by IR$^{\Delta GFAP}$ mice. Acute intracerebroventricular administration of 2-methylthio-ATP (2-MeSATP), a nonselective P2 purinergic agonist (Fig. 7C), was sufficient for IR$^{\Delta GFAP}$ mice to recover control mice–like suppression of hyperphagia in NCD (fig. S8Q) and in HFD (Fig. 7D), which was absent in vehicle-treated

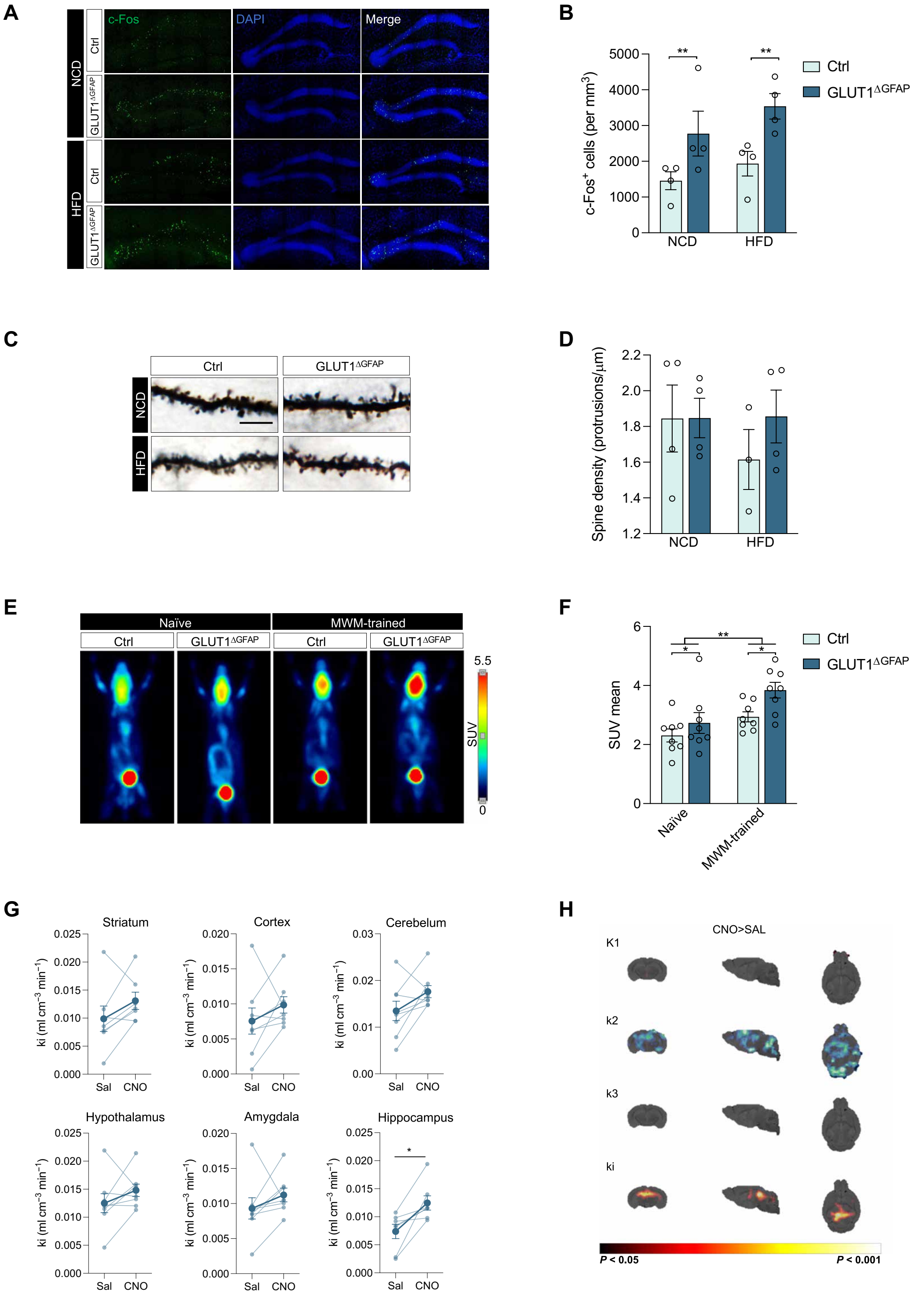

Fig. 5. Enhanced neuronal activation and brain glucose metabolism in GLUT1$^{\Delta GFAP}$ mice upon astrocytic stimulation. (**A**) Representative c-Fos (green) staining in the dentate gyrus of the hippocampus and (**B**) quantification of c-Fos^{+} cells per area in Ctrl and GLUT1$^{\Delta GFAP}$ mice under NCD or HFD ($n = 4$ mice per group and 2 slices per mouse). (**C**) Representative image of dendritic spines from Golgi-Cox–stained slices and (**D**) quantification of the spine density from NCD- and HFD-fed Ctrl and GLUT1$^{\Delta GFAP}$ mice ($n = 4$ mice per group and 30 dendrites per animal). (**E**) PET images of representative mice showing brain ^{18}F-FDG signal and (**F**) the quantification of positron emission (mean SUV) of naïve and MWM-trained Ctrl and GLUT1$^{\Delta GFAP}$ mice ($n = 8$ mice per group). (**G**) Representation of the ki constant of glucose kinetics before and after CNO activation in different brain areas and (**H**) comparison of PET images of all constants confirming that ki is significantly elevated in the hippocampus after CNO activation. In (G), light lines represent each individual mouse, while the dark line represent the mean ± SEM ($n = 7$ mice per group). Data are presented as means ± SEM. $^{*}P \leq 0.05$ and $^{**}P \leq 0.01$, as determined by two-way ANOVA followed by Tukey (B, D, and F) and two-tailed Student's *t* test (G).

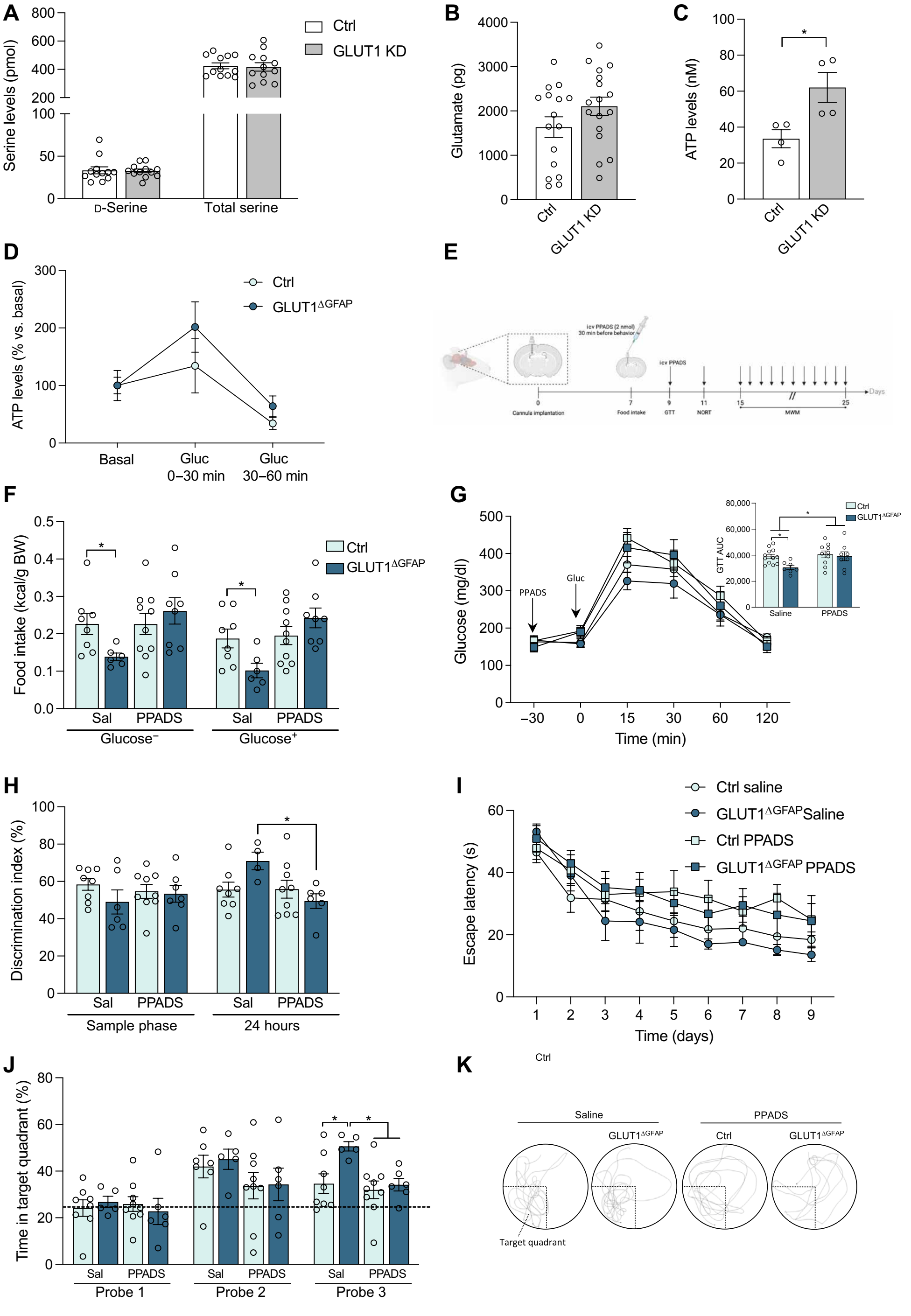

Fig. 6. Essential role of brain purinergic signaling in the phenotype exhibited by astrocytic GLUT1-ablated mice. (**A**) D- and total serine, (**B**) glutamate, and (**C**) ATP release from Ctrl and GLUT1 KD primary cell–cultured astrocytes ($n = 4$ to 12 independently isolated astrocyte cultures). (**D**) ATP levels in microdialysis-isolated interstitial fluid of Ctrl and GLUT1$^{\Delta GFAP}$ mice before (basal) and after intraperitoneal glucose injection (0 to 30 and 30 to 60 min). Data were expressed as the percentage of their own basal ($n = 8$ to 10 mice per group). (**E**) Schematic illustration of intracerebroventricular (icv) cannulation and PPADS intracerebroventricular administration 30 min before each metabolic and cognitive assessment task. Created with BioRender.com. (**F**) Glucose-induced suppression of feeding evaluated by 4-hour accumulated food intake in Ctrl and GLUT1$^{\Delta GFAP}$ mice subjected to HFD after saline or PPADS intracerebroventricular injection ($n = 6$ to 10 per group). (**G**) GTT in saline-treated or PPADS intracerebroventricularly treated Ctrl and GLUT1$^{\Delta GFAP}$ mice on HFD and AUC quantification ($n = 7$ to 12 per group). (**H**) Recognition memory assessment by NOR task of HFD-fed Ctrl and GLUT1$^{\Delta GFAP}$ mice after saline or PPADS intracerebroventricular administration ($n = 6$ to 9 per group). (**I**) Spatial memory evaluation by MWM acquisition phase, (**J**) retention phase, and (**K**) a representative image of the swimming path of saline-treated or PPADS intracerebroventricularly treated Ctrl and GLUT1$^{\Delta GFAP}$ mice on HFD ($n = 5$ to 9 per group). Data are presented as means ± SEM. *$P \leq 0.05$, as determined by two-tailed Student's *t* test (A to C), repeated-measurement ANOVA (D, G, and I) and two-way ANOVA followed by Tukey [(F and G) AUC and (H and J)].

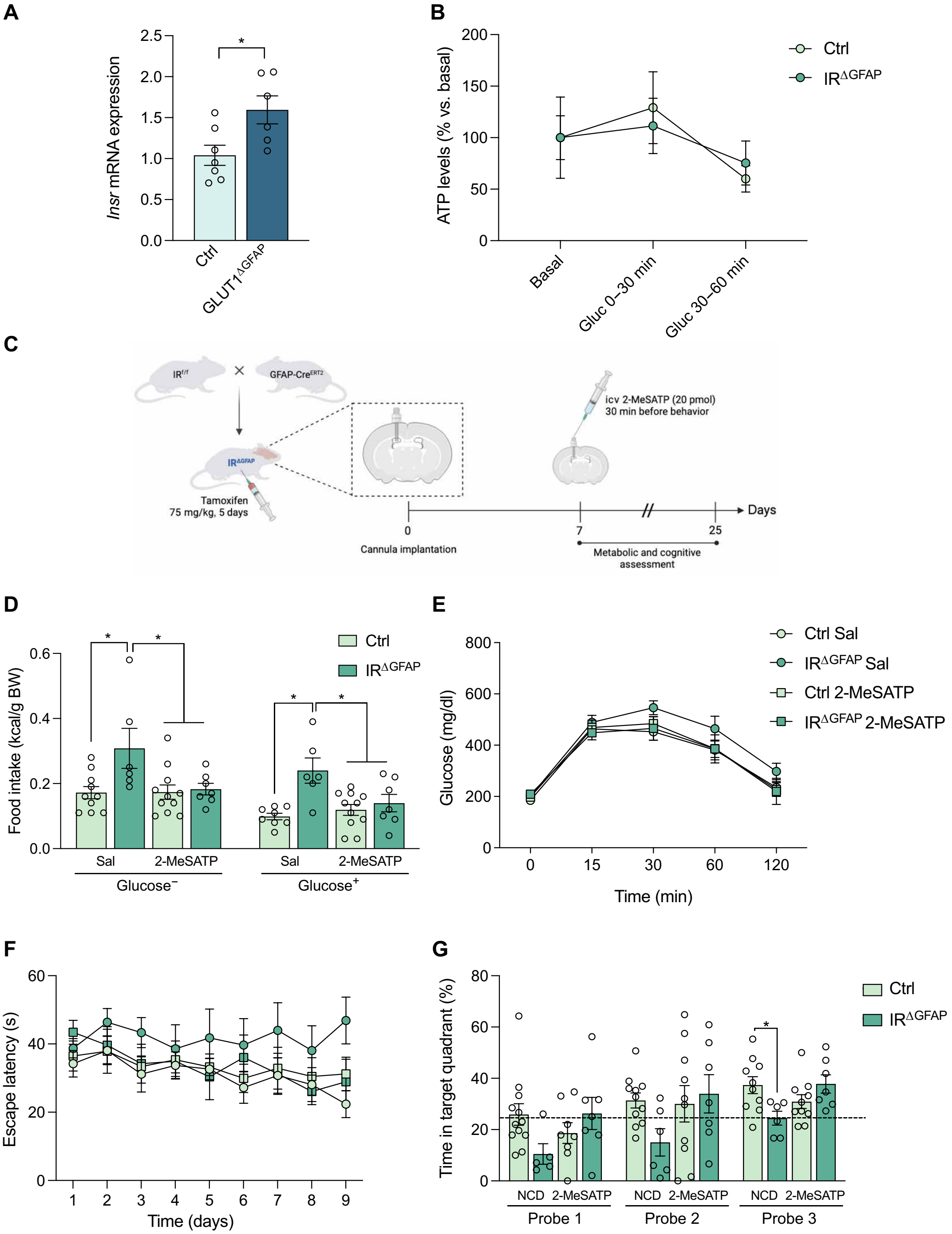

Fig. 7. Astrocytic insulin receptor depletion-induced alterations are rescued by purinergic signaling enhancement. (**A**) *Insr* (IR, encoding gene) mRNA levels in Ctrl and GLUT1$^{\Delta GFAP}$ mice after ACSA-2$^+$ FACS-mediated isolation of astrocytes ($n = 6$ mice per group). (**B**) ATP levels in microdialysis-isolated interstitial fluid of Ctrl and IR$^{\Delta GFAP}$ mice before (basal) and after intraperitoneal glucose injection (0 to 30 and 30 to 60 min). Data are expressed as the percentage of their own basal ($n = 6$ to 8 mice per group). (**C**) Schematic illustration of the strategy used to generate mice lacking IR specifically in astrocytes (IR$^{\Delta GFAP}$) and their Ctrl littermates (IR$^{f/f}$), intracerebroventricular cannulation, and 2-MeSATP intracerebroventricular administration. Created with BioRender.com. (**D**) Glucose-induced suppression of feeding evaluated by 4-hour accumulated food intake in Ctrl and IR$^{\Delta GFAP}$ mice subjected to HFD after saline or 2-MeSATP intracerebroventricular injection ($n = 6$ to 11 per group). (**E**) GTT in saline-treated or 2-MeSATP intracerebroventricularly treated Ctrl and IR$^{\Delta GFAP}$ mice on HFD ($n = 8$ to 12 per group). (**F**) Spatial memory evaluation by MWM acquisition and (**G**) retention phase of saline-treated or 2-MeSATP intracerebroventricularly treated Ctrl and IR$^{\Delta GFAP}$ mice on HFD ($n = 5$ to 12 per group). Data are presented as means ± SEM. $*P \leq 0.05$ as determined by two-tailed Student's *t* test (A), repeated-measurement ANOVA (B, E, and F), and two-way ANOVA followed by Tukey (D and G).

IR$^{\Delta GFAP}$ mice. 2-MeSATP administration also reverted the glucose intolerance shown by IR$^{\Delta GFAP}$ mice [NCD (fig. S8R) and HFD (Fig. 7E)]. Furthermore, the impairments in spatial memory abilities exhibited by vehicle-treated IR$^{\Delta GFAP}$ mice were corrected upon intracerebroventricular 2-MeSATP treatment in NCD (fig. S8, S and T) and in HFD (Fig. 7, F and G). Together, these results provide the first evidence of the relevance of astrocytic IR for spatial memory and demonstrate that brain-specific purinergic stimulation is sufficient to rescue the aberrant glucose metabolism and cognitive deficits elicited by astrocyte-specific IR decrease.

Enhanced astrocytic insulin signaling in GLUT1-ablated astrocytes is indispensable for improved glucose homeostasis and memory preservation

In line with above-mentioned evidence of a higher IR expression in GLUT1-deficient astrocytes, an enhanced insulin-stimulated ATP release was observed in cultured GLUT1 KD astrocytes, and this effect was totally abrogated by concomitant treatment with S961, a specific IR antagonist (Fig. 8A). Besides, insulin treatment did not trigger an increased ATP release in cultured IR KD astrocytes, confirming the necessity of IR for insulin-stimulated ATP release (Fig. 8A).

Taking all these data into consideration, we examined whether insulin signaling is necessary for the metabolic and cognitive improvements observed in GLUT1$^{\Delta GFAP}$ mice. Acute intracerebroventricular S961 administration blunted the improved fasting-induced hyperphagia [NCD (fig. S9A) and HFD (Fig. 8B)] and enhanced glucose tolerance found in GLUT1$^{\Delta GFAP}$ mice [NCD (fig. S9B) and HFD (Fig. 8C)]. These results evidence that GLUT1$^{\Delta GFAP}$ mice require fully operative brain insulin signaling to display their improved systemic glucose homeostasis. However, considering that S961 can antagonize the IR present in most brain cell types (*10*), these data are unable to differentiate the specific contribution of astrocytic IR to the phenotype of GLUT1$^{\Delta GFAP}$ mice. To address this relevant question, we crossed IR$^{\Delta GFAP}$ with GLUT1$^{\Delta GFAP}$ mice to generate hGFAP-CreER$^{T2+/-}$:*Slc2a1*$^{f/f}$:*Insr*$^{f/f}$ (named GLUT1-IR$^{\Delta GFAP}$) mice, in which tamoxifen administration induces concomitant depletion of GLUT1 and IR exclusively from astrocytes (Fig. 8D). First, microdialysis experiments showed that GLUT1-IR$^{\Delta GFAP}$ failed to increase brain ATP levels upon intraperitoneal glucose injection (Fig. 8E) to the same extent as GLUT1$^{\Delta GFAP}$ mice. Moreover, ^{18}F-FDG–PET studies revealed that GLUT1-IR$^{\Delta GFAP}$ mice not only lacked the characteristic that enhanced ^{18}F-FDG signal present in GLUT1$^{\Delta GFAP}$ mice but also featured diminished brain glucose utilization similar to what is observed upon isolated IR deficiency (Fig. 8, F and G, and fig. S9, C to F). Besides, concomitant depletion of IR and GLUT1 in astrocytes, without inducing body weight differences (fig. S9G), abolished the beneficial effects regarding both food intake (Fig. 8H) and glucose tolerance observed in GLUT1$^{\Delta GFAP}$ mice (Fig. 8I), without altering insulin sensitivity (Fig. 8J). Last, GLUT1-IR$^{\Delta GFAP}$ mice failed to maintain the spatial memory acquisition (Fig. 8K) and retention (Fig. 8L) observed in GLUT1$^{\Delta GFAP}$ mice, in the absence of locomotor activity alterations (fig. S9H).

Provided that the effects of astrocytic IR reduction were rescued by acute intracerebroventricular administration of the 2-MeSATP, we decided to treat GLUT1-IR$^{\Delta GFAP}$ mice with this same compound. Crucially, intracerebroventricular administration of 2-MeSATP was sufficient to revert both the inability to properly control peripherally induced hyperglycemia [NCD (fig. S9I) and HFD (Fig. 8M)] and the memory deficits shown by GLUT1-IR$^{\Delta GFAP}$ mice [NCD (fig. S9, J and K) and HFD (Fig. 8, N and O)].

Together, these results indicate that enhanced IR expression in GLUT1$^{\Delta GFAP}$ mice is a necessary feature to improve glucose homeostasis and to maintain memory. In addition, these results also show that brain-specific purinergic stimulation is sufficient to rescue the metabolic and cognitive deficits induced upon concomitant GLUT1 and IR depletion in astrocytes.

DISCUSSION

It is well established that GLUT1 is the transporter mediating glucose access across the BBB into the brain. Particularly, the lethality of mice with inducible ablation of GLUT1 in the BBB vascular endothelial cells has highlighted the crucial role for endothelial GLUT1 expression in the control of brain glucose uptake and energetics (*55*, *56*). Astrocytic GLUT1-containing endfeet cover almost the entire surface of the blood vessels (*57*) with over than 99% of the astrocytes being connected to blood vessels (*58*). Given these features and the well-accepted ANLS hypothesis, according to which astrocytes must metabolize glucose and export lactate to neurons for the latter to meet energy needs (*14*), one could hypothesize that ablating GLUT1, the main GLUT expressed in these cells, would lead to a breakdown of brain glucose uptake and metabolism. Against these expectations, our data indicate that a partial astrocytic GLUT1 reduction results in a paradoxical enhancement of brain glucose utilization. In light of the decreased glycolysis observed upon GLUT1 decline in cultured astrocytes together with the finding that both astrocytic glucose uptake and glycolytic pathway usage are significantly reduced in vivo upon GLUT1 diminishment, it is tempting to speculate that other brain cell types could be responsible for the increased glucose metabolism observed in GLUT1$^{\Delta GFAP}$ mice. This idea has been already suggested by modeling studies predicting that most of the glucose diffuses from endothelial cells independently of astrocytic endfeet and throughout the extracellular fluid to more distant brain cells, facilitating rapid GLUT3-mediated uptake into neurons (*13*). The validity of this model has been elegantly proven in vivo, showing that upon stimulation, glucose consumption by neurons is markedly increased, shifting to a highly glycolytic profile to account for the elevated energy demand (*20*). However, compelling criticisms of the current interpretation of these studies are the following: (i) One of the above-mentioned studies was conducted primarily on a highly specialized type of neuron (dentate granule cells of the hippocampus) that constitutes a minority of the brain's neuronal population and exhibits a unique morphology that is significantly different from most cortical or hippocampal neurons. (ii) The other study was based on kinetic parameters taken from granule cerebellar cells that can behave in a very different manner compared to other cell types, and (iii) it is presumptuous to assume that neuronal glucose, taken up in an activity-dependent manner, is metabolized primarily through glycolysis. Specifically, glucose uptake does not necessarily imply glycolytic metabolism. Instead, neuronal stimulation may preferentially direct glucose metabolism through the pentose phosphate pathway (PPP), aligning with the established view of neurons as cells with limited glycolytic activity. Crucially, research has shown that neurons undergo continuous degradation of 6-phosphofructo-2-kinase/fructose-2,6-bisphosphatase-3, thereby actively suppressing glycolysis and promoting glucose oxidation via

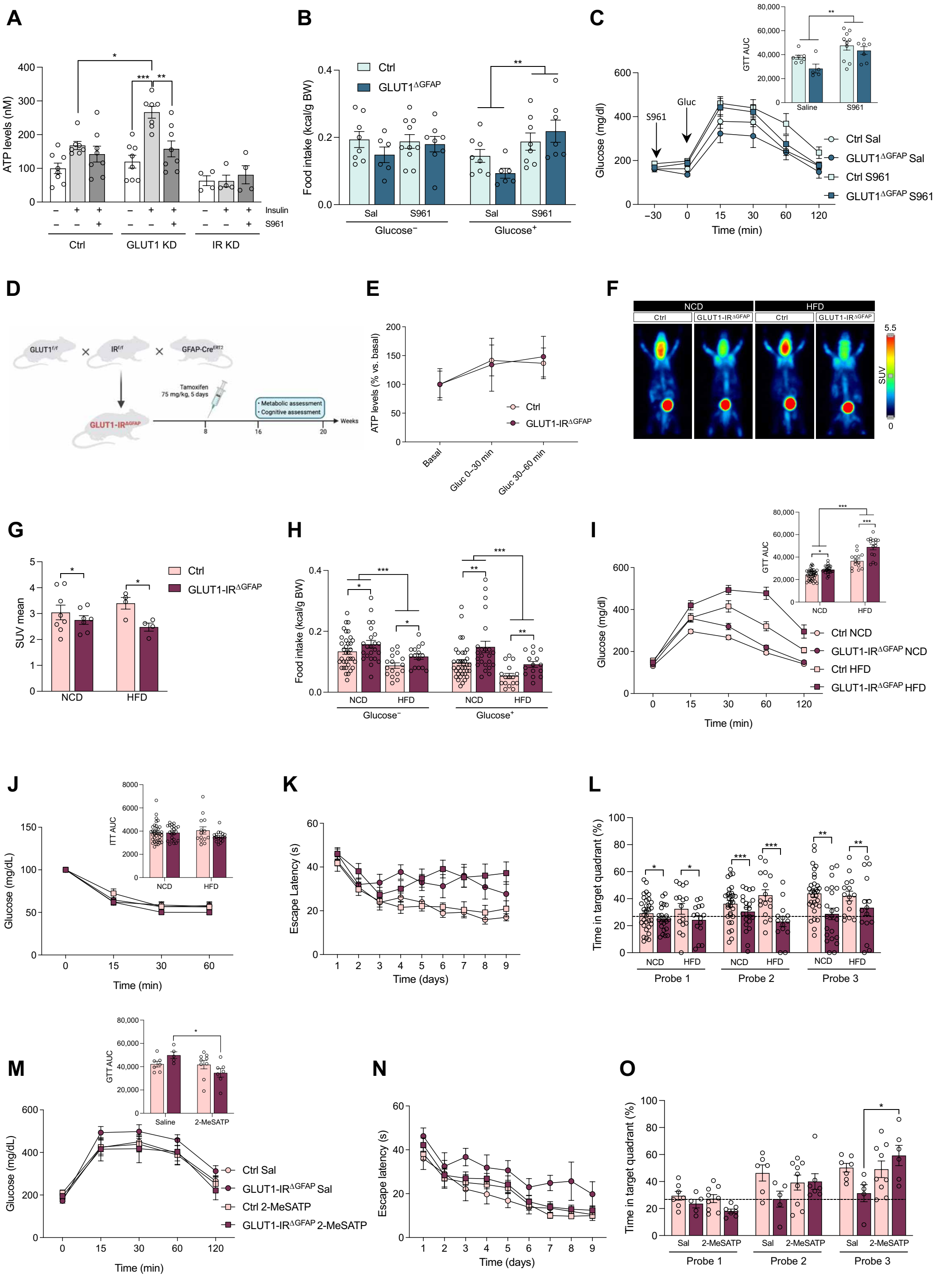

Fig. 8. Increased astrocytic insulin receptor signaling is necessary for the ATP signaling-mediated benefits of astrocytic GLUT1 depletion. (**A**) ATP release from Ctrl, GLUT1 KD, and IR KD astrocytes exposed to either vehicle, insulin, or insulin + S961 (IR antagonist; $n = 4$ independently isolated astrocyte cultures). (**B**) Four-hour accumulated food intake in Ctrl and GLUT1$^{\Delta GFAP}$ mice subjected to HFD after saline or S961 intracerebroventricular injection ($n = 6$ to 10). (**C**) GTT in saline-treated or S961 intracerebroventricularly treated mice on HFD and the corresponding AUC quantification ($n = 5$ to 10). (**D**) Strategy used to generate mice concomitantly lacking GLUT1 and IR specifically in astrocytes (GLUT1-IR$^{\Delta GFAP}$). Created with BioRender.com. (**E**) ATP levels in microdialysis-isolated interstitial fluid before (basal) and after intraperitoneal glucose injection (0 to 30 and 30 to 60 min; $n = 8$). (**F**) PET images of representative mice showing brain ^{18}F-FDG signal and (**G**) the quantification (mean SUV; $n = 4$ to 8 mice). (**H**) Glucose-induced suppression of feeding, (**I**) GTT with AUC, and (**J**) insulin tolerance test with AUC ($n = 15$ to 30). (**K**) Spatial memory evaluation by MWM acquisition and (**L**) retention phase ($n = 15$ to 30). (**M**) GTT in saline-treated or 2-MeSATP intracerebroventricularly treated Ctrl and GLUT1-IR$^{\Delta GFAP}$ mice on HFD ($n = 5$ to 9). (**N**) MWM acquisition and (**O**) retention phase of saline-treated or 2-MeSATP intracerebroventricularly treated mice on HFD ($n = 5$ to 9). Data are presented as means ± SEM. $^{*}P \le 0.05$, $^{**}P \le 0.01$, and $^{***}P \le 0.001$, as determined by two-way ANOVA followed by Tukey [(A to C) AUC, (G to I) AUC, (J) AUC, (L and M) AUC, and O] and repeated-measurement ANOVA (C, E, I, J, K, M, and N).

the PPP, as it has been elegantly demonstrated by studies conducted by J. P. Bolaños' group (*59*, *60*).

In addition to the neuronal hypothesis, microglial cells have been identified as central regulators of the ^{18}F-FDG–PET brain signal. Microglia adopt a glycolytic phenotype under inflammatory activation (*61*–*63*), and recent studies show that microglial glucose uptake exceeds that of neurons and astrocytes in various neurodegenerative disease models (*64*). Although this increased uptake is observed in neurodegeneration, it raises the possibility that microglial states influence brain glucose metabolism even in healthy brains. While the present study did not assess microglial activity, it is plausible that heightened microglial activity could contribute to the enhanced ^{18}F-FDG–PET signal in GLUT1$^{\Delta GFAP}$ mice brains.

Consideration must be given to another prominent glycolytic cell type: oligodendroglia. Oligodendrocytes exhibit high glycolytic activity, with their glycolytic products rapidly metabolized in white matter tracts (*65*). Notably, activation of oligodendroglial *N*-methyl-D-aspartate receptors (NMDAR) by glutamate enhances both GLUT1 presence in the oligodendrocyte plasma membrane and glucose import. This mechanism allows oligodendrocytes to transfer glycolysis-derived lactate to neuronal axons, thereby supporting axonal energy metabolism (*66*). Consequently, it is plausible that oligodendrocytes could up-regulate GLUT1 following astrocytic GLUT1 ablation, compensating for the glucose uptake deficiency in astrocytes and thus explaining the enhanced brain glucose metabolism observed in GLUT1$^{\Delta GFAP}$ mice. In this context, oligodendrocytes would likely increase the donation of glycolytic-derived lactate to axons, improving axonal energy efficiency. This enhanced energy efficiency could support increased neuronal activity without inducing metabolic stress, thereby explaining the heightened neuronal activity observed in the brains of GLUT1$^{\Delta GFAP}$ mice.

Ultimately, whether glucose consumption is elevated by neurons, microglia, oligodendrocytes, or a combination of these and/or other cells, our findings underscore the pivotal role of astrocytic GLUT1 in maintaining brain energy homeostasis. Our discoveries that brain glucose metabolism is not simply maintained but enhanced in GLUT1$^{\Delta GFAP}$ mice and that a network of energy metabolism–related proteins is shifted in our proteomic profiling indicates that astrocytic GLUT1 is important enough to trigger a reprogramming of the overall brain metabolism sufficient to sustain energy requirements upon its depletion.

Moreover, mice lacking GLUT1 in astrocytes exhibited improved abilities regarding glucose homeostasis. Glucose-sensing POMC neurons in the ARC are well established as central mediators of satiety (*67*), being also able to regulate insulin secretion (*38*) and glucose metabolism (*36*, *68*). POMC neuron glucose sensitivity becomes impaired in HFD-induced obesity, losing their glucose homeostasis regulatory properties (*68*). Previous studies have reported that alterations in the glial distribution surrounding hypothalamic POMC neurons can influence their ability to respond to glucose fluctuations (*39*). Likewise, glucose-sensing TH neurons in the locus coeruleus increase body energy expenditure during HFD-induced obesity by prompting BAT activation (*40*). Our data reveal that, particularly, HFD-fed animals benefit from astrocytic GLUT1 reduction, exhibiting enhanced glucose homeostasis in comparison to HFD-fed control animals. Provided that the loss of GLUT1 specifically in astrocytes of HFD-fed animals induced enhanced glucose-stimulated activation of both ARC POMC neurons and locus coeruleus TH neurons, this leads us to argue that astrocytic GLUT1 decrease ameliorated the glucose sensing of these neuronal populations that could be linked to the observed lower astrocytic synaptic coverage, highlighting its importance of these neuronal populations in the activation of peripheral processes that facilitate glucose metabolism such as insulin secretion or BAT activity, respectively.

Brain glucose metabolism and cognitive proficiency are intimately correlated (*42*, *43*). Although it has been established that astrocytic lactate is needed for memory formation (*33*) and that BBB endothelial cell GLUT1 ablation triggers cognitive breakdown (*34*), the necessity of astrocytic GLUT1 for cognitive performance has never been tested. Notably, far from experiencing a cognitive breakdown, mice lacking GLUT1 in astrocytes were able to form and retain memories, even showing both more active hippocampal neurons and cognitive task–elicited brain glucose metabolism in PET studies compared to control mice. All of these features can be considered as a readout of healthy memory neurocircuits, arguing against the presupposition that astrocytic GLUT1 is as necessary as endothelial GLUT1 to fuel cognitive abilities and against the necessity of astrocytic glycolysis for memory formation.

In light of the metabolic and cognitive improvement observed, which could be directly linked to the enhanced POMC and hippocampal neuronal activation (as reflected by increased c-Fos activity), our hypothesis arguing for the improved neuronal glucose metabolism upon astrocytic GLUT1 deficiency became potentially more relevant. Specific increased hippocampal PET signal following astrocytic chemogenetic activation of astrocytes in that area points toward the same conclusion. Pursuing this idea, we speculated that GLUT1$^{\Delta GFAP}$ astrocytes could be communicating more efficiently with other surrounding cells. Astrocytes convey information to neighboring cells via the release of gliotransmitters (*49*). We found that GLUT1 KD resulted in an enhanced capacity of astrocytes to release ATP. It has been described that IR activation by insulin in astrocytes mediates ATP exocytosis (*48*), and we found elevated IR levels in GLUT1-ablated astrocytes, which were responsible for maintaining astrocytic insulin-dependent ATP release. Thus, both the combination of enhanced glucose-stimulated insulin release and astrocytic IR overexpression may cooperate to elicit higher ATP release. This model is further supported by our data, indicating that the beneficial effect of astrocyte GLUT1 reduction is reversed by both the inhibition of purinergic signaling and simultaneous IR depletion, the effect of which can be overcome by the activation of purinergic signaling.

Collectively, this study uncovered a central role of astrocytes orchestrating brain energy metabolism. Specifically, astrocytic GLUT1 reduction induces an "astrocytic glucose scarcity" situation with lower astrocytic glucose uptake and glycolysis. In this scenario, a fundamental astrocytic reprogramming is conducted with IR overexpression and improved ATP release. Further, the enhanced purinergic signaling could propagate direct or indirect signals to neurons (and/or other brain cells), indicating the necessity of a higher metabolic rate (that could be obtained from higher glucose metabolism) and inducing its activity, which is translated into improved peripheral energy metabolism and preserved cognition.

Understanding this astrocytic energetic reprogramming upon glycolytic scarcity could open unexplored horizons for the treatment of central and peripheral diseases, for instance, obesity and neurodegenerative disorders, which course with energetic alterations. Those diseases intimately related to a "brain energy gap," are often improved with alternative diets such as ketogenic diets, which cause reductions on the brain's reliance on glucose as a fuel. However, the negative long-term consequences of ketogenic diets (especially in the periphery) may far outweigh any potential short-term benefits (*69*). In this scenario, we offer a vision where the beneficial effect of decreased glucose availability could be achieved by limiting the glucose uptake only in a specific brain cell type, i.e., astrocytes. Therefore, we propose the astrocytic decreased glycolytic capacity as a future therapeutic approach for energetic diseases such as obesity or neurodegeneration.

MATERIALS AND METHODS

Genetic mouse models

GLUT1$^{f/f}$ mice

Slc2a1$^{flox/flox}$ (named GLUT1$^{f/f}$) mice (*70*) were provided by J.C.B. (Max Planck Institute for Metabolism Research, Cologne, Germany), with the permission of G.K. (Columbia University, NY, USA).

IR$^{f/f}$ mice

Insr$^{flox/flox}$ (named IR$^{f/f}$) mice (*71*) were purchased from The Jackson Laboratory [B6.129S4(FVB)-Insr^{tm1Khn}/J; strain# 006955; RRID:IMSR_JAX:006955].

hGFAP-CreER^{T2} mice

hGFAP-CreER^{T2} mice (*72*) were purchased from The Jackson Laboratory [B6.Cg-Tg(GFAP-cre/ERT2)505Fmv/J; strain# 012849; RRID:IMSR_JAX:012849].

GLUT1$^{\Delta GFAP}$ mice

hGFAP-CreER^{T2} mice were mated with GLUT1$^{f/f}$ mice to obtain hGFAP-CreER^{T2}:GLUT1$^{f/f}$ mice (named GLUT1$^{\Delta GFAP}$), and subsequently, breeding colonies were maintained by mating GLUT1$^{f/f}$ mice with hGFAP-CreER^{T2}:GLUT1$^{f/f}$ mice. The hGFAP-CreER^{T2} allele was maintained in heterozygous conditions, whereas the floxed GLUT1 allele was maintained in homozygous conditions. Animals were kept on a C57BL/6J background. Cre-dependent depletion of the floxed GLUT1 allele was accomplished by tamoxifen (Sigma-Aldrich, #T5648) administration [75 mg/kg, intraperitoneally (ip), every 24 hours for 5 consecutive days] at 8 weeks of postnatal age, as described below (see the "Tamoxifen treatment" section).

IR$^{\Delta GFAP}$ mice

hGFAP-CreER^{T2} mice were mated with IR$^{f/f}$ mice to obtain hGFAP-CreER^{T2}:IR$^{f/f}$ mice (named IR$^{\Delta GFAP}$), and subsequently, breeding colonies were maintained by mating IR$^{f/f}$ mice with hGFAP-CreER^{T2}:IR$^{f/f}$ mice. The hGFAP-CreER^{T2} allele was maintained in heterozygous conditions, whereas the floxed IR allele was maintained in homozygous conditions. Animals were kept on a C57BL/6J background. Cre-dependent depletion of the floxed IR allele was accomplished by tamoxifen (Sigma-Aldrich, #T5648) administration (75 mg/kg, ip, every 24 hours for 5 consecutive days) at 8 weeks of postnatal age, as described below (see the "Tamoxifen treatment" section).

GLUT1-IR$^{\Delta GFAP}$ mice

hGFAP-CreER^{T2}:GLUT1$^{f/f}$ mice were mated with IR$^{f/f}$ mice to obtain hGFAP-CreER^{T2}:GLUT1$^{f/f}$:IR$^{f/f}$ mice (named GLUT1-IR$^{\Delta GFAP}$), and subsequently, breeding colonies were maintained by mating GLUT1$^{f/f}$:IR$^{f/f}$ mice with hGFAP-CreER^{T2}:GLUT1$^{f/f}$:IR$^{f/f}$ mice. The hGFAP-CreER^{T2} allele was maintained in heterozygous conditions, whereas the floxed GLUT1 and floxed IR alleles were maintained in homozygous conditions. Animals were kept on a C57BL/6J background. Cre-dependent depletion of the floxed GLUT1 and IR alleles was accomplished by tamoxifen (Sigma-Aldrich, #T5648) administration (75 mg/kg, ip, every 24 hours for 5 consecutive days) at 8 weeks of postnatal age, as described below (see the "Tamoxifen treatment" section).

Tamoxifen treatment

To excise LoxP sites by Cre recombination, 8-week-old hGFAP-CreER^{T2}:GLUT1$^{f/f}$, hGFAP-CreER^{T2}:IR$^{f/f}$, and hGFAP-CreER^{T2}:GLUT1$^{f/f}$:IR$^{f/f}$ mice were subjected to tamoxifen administration. Briefly, tamoxifen was dissolved at 55°C in a 10% ethanol–90% peanut oil (Sigma-Aldrich, #P2144) solution at a concentration of 20 mg/ml. This solution was used to inject mice tamoxifen (75 mg/kg, ip) daily for 5 consecutive days. To maintain the same experimental conditions, all the corresponding control groups (GLUT1$^{f/f}$, IR$^{f/f}$ and GLUT1$^{f/f}$:IR$^{f/f}$) also received the tamoxifen treatment.

Animal care

All animal procedures were conducted in compliance with the European and Spanish regulations (2003/65/EC; 1201/2005) for the care and use of laboratory animals and approved by the ethical committee of the University of Navarra (ethical protocol number 076-19).

Primary mouse astrocyte cultures

Astrocyte isolation and culture

Astrocytes from the hippocampi, hypothalami, and cortices were isolated from GLUT1$^{f/f}$ or IR$^{f/f}$ mice pups at postnatal day 0 to 4 to perform astrocytic primary cell cultures. For a detailed method, see Supplementary Text.

Astrocyte transfection and selection

Astrocytes were transfected with either control plasmid ("pCMV-Myc-GFP" plasmid; Addgene, #83375) or pCMV-Cre-GFP (green fluorescent protein) plasmid ("Cre Shine" plasmid; Addgene, #37404). For detailed methods, see Supplementary Text.

Real-time cell metabolic analysis

Extracellular metabolic flux dynamics were measured in primary astrocytes using the XFp Extracellular Flux Analyzer ("Seahorse," Agilent Technologies). The day before the assay, astrocytes were seeded in XFp plates at a density of 20,000 cells per well and maintained in complete culture medium for 24 hours. Thereafter, 1 hour before the assay, cells were transferred to Seahorse XF DMEM Medium (Agilent Technologies) supplemented with 10 mM glucose, 2 mM glutamine, and 1 mM pyruvate and were kept in this medium during the whole assay. All results were normalized by protein content, which was quantified using the Bio-Rad Protein Assay (Bio-Rad) according to the manufacturer's instructions.

With this technology, mitochondrial respiration and glycolysis, glycolytic rate and ATP production, fuel dependency, and glutamine capacity were evaluated (for detailed methods, see Supplementary Text).

L-Lactate release

L-lactate release was assessed with the EnzyChrom Lactate Assay Kit (BioAssay Systems, #ECLC-100) following the manufacturer's instructions (for detailed methods, see Supplementary Text).

2-Deoxyglucose uptake

Glucose uptake by cultured primary astrocytes was studied using the colorimetric Glucose Uptake Assay Kit (Abcam, #ab136955) according to the manufacturer's instructions (for detailed methods, see Supplementary Text).

ATP determination

To assess the ability of primary astrocytes to release ATP and the ATP content in in vivo microdialysed samples, the luciferase-based ATP Determination Kit (Invitrogen, #A22066) was used following the manufacturer's instructions (for detailed methods, see Supplementary Text).

Serine release determination

The ability of primary astrocytes to release serine was evaluated using the fluorescent DL-Serine Assay Kit (Abcam, #ab241027) following the manufacturer's instructions (for detailed methods, see Supplementary Text).

Glutamate release determination

The ability of primary astrocytes to release glutamate was measured using high-performance liquid chromatography with electrochemical detection (DECADE, Antec Leyden; for detailed methods, see Supplementary Text).

^{18}F-FDG–PET

Static PET studies

2-Deoxy-2-[^{18}F]fluoro-D-glucose (^{18}F-FDG) and PET were used to assess brain glucose metabolism. Briefly, mice were fasted overnight, and the following morning, ^{18}F-FDG [9.5 millionbecquerel (MBq) ± 0/6 in 80 to 100 μl] was injected intravenously. After an uptake period of 50 min, mice were anesthetized with 2% isoflurane in 100% O_2 gas and placed in a small PET tomograph (Mosaic, Philips). Mice were subsequently subjected to a 15-min PET acquisition. Images were reconstructed, applying dead time, decay, and random and scattering corrections. Images were semiquantitatively analyzed using the PMOD v3.2 software (PMOD Technologies Ltd.), expressing values in standardized uptake value (SUV) units, using the formula SUV = [tissue activity concentration (Bq/cm^3)/injected dose (Bq)] × body weight (g). ^{18}F-FDG metabolism was assessed by drawing two spherical volumes of interest (VOIs) for each image, including the entire brain and the reference organ (liver). Semiautomatic delineation was applied with a threshold of 50% of the maximum or minimum voxel value to obtain new VOIs that delimited brain or the reference organ, respectively. The average SUV (SUV_{mean}) of the voxels within the VOIs was calculated, and SUV_{mean} ratios were calculated by dividing brain SUV_{mean} by reference organ SUV_{mean}. After PET acquisition, mice were euthanized, and their brains were dissected to assess ex vivo radiotracer incorporation across brain areas (hypothalamus, hippocampus, frontal cortex, and cerebellum). A gamma counter (Hidex Automatic Gamma Counter, Hidex Oy) was used to perform ex vivo counting of radioactivity in the samples, which were dissected by the same experimenter and corrected by sample weight. Ex vivo radiotracer incorporation was expressed as percentage of the injected dose.

dPET studies

dPET/CT (computed tomography) studies were acquired using a small animal PET/CT scanner (Albira ARS PET/CT dual scanner, Bruker, Spain) for 60 min. The animals' blood glucose levels were measured before catheterizing the lateral tail vein by inserting a 34-gauge needle connected to a cannula. CNO (3 mg/kg, ip) or saline (intraperitoneally) was injected 10 min before the tracer ^{18}F-FDG (6.14 MBq in 200 μl, intravenously; Curium Pharma, Madrid), while the animals were under inhalation anesthesia (2% isoflurane in oxygen flow of 1 liter/min). All images were reconstructed using the maximum likelihood expectation maximization (MLEM) algorithm. The iterative reconstruction of the PET data comprises 32 frames of 5 × 2 s, 4 × 5 s, 3 × 10 s, 8 × 30 s, 5 × 60 s, 4 × 300 s, and 3 × 600 s.

A two-compartment FDG kinetic model was used to analyze the dynamics of ^{18}F-FDG in the brain. Along with the VOIs of the different brain areas, another spherical VOI of the vena cava (3 mm) was created in the sixth frame of each animal to determine the blood input function, and its time-activity curve was fitted to a three-exponential whole-blood model. The model was evaluated by applying a lumped constant of 0.67 and the corresponding plasma glucose levels (in mM) of each animal. The hippocampal VOI time-activity curve was corrected by minimizing chi-square values and fitted to whole blood, with blood volume fraction set to physiological levels (vB = 2%). The kinetic parameter K1 (ml min^{-1} ml^{-1}) represents the transport rate of ^{18}F-FDG from the arterial plasma to the intercellular space and k2 (1/min), the opposite direction. k3 (1/min) represents the phosphorylation of ^{18}F-FDG inside cells, and in this particular model, the dephosphorization rate is not considered (k4 = 0). In addition, this model includes a rate constant that indicates the flow of the radiotracer through the two compartments (ki).

In vivo U-^{13}C-glucose isotope tracing

U-^{13}C-glucose infusion

Nonradioactive ^{13}C-labeled glucose (0.8 M) was infused through the femoral vein at a steady rate of 4 μl/min over the course of 3 hours, while the mice were anesthetized with isoflurane. After 2 hours, mice were euthanized, and astrocytes were isolated by flow cytometry (see the "Fluorescence-activated cell sorting" section) and processed by liquid chromatography–mass spectrometry (LC-MS) for measurement of metabolites.

LC-MS measurement of metabolites

The LC-MS method involved hydrophilic interaction chromatography coupled to the Q Exactive Plus mass spectrometer (Thermo Fisher Scientific). The LC separation was performed on a XBridge BEH Amide column (150 mm × 2.1 mm, 2.5-μm particle size; Waters). Solvent A is 95%:5% H2O:acetonitrile with 20 mM ammonium bicarbonate, and solvent B is acetonitrile. The gradient was 0 min, 85% B; 2 min, 85% B; 3 min, 80% B; 5 min, 80% B; 6 min, 75% B; 7 min, 75% B; 8 min, 70% B; 9 min, 70% B; 10 min, 50% B; 12 min, 50% B; 13 min, 25% B; 16 min, 25% B; 18 min, 0% B; 23 min, 0% B; 24 min, 85% B; and 30 min, 85% B. Other LC parameters were as follows: flow rate, 150 ml/min; column temperature, 25°C; injection volume, 10 ml; and autosampler temperature, 5°C. The mass spectrometer was operated in both negative- and positive-ion mode for the detection of metabolites. Other MS parameters were as follows: resolution of 140,000 at a mass/charge ratio (m/z) of 200, automatic gain control target at 3×10^6, maximum injection time of 30 ms, and scan range of m/z of 75 to 1000. Data were analyzed using MAVEN software, and isotope labeling was corrected for natural ^{13}C abundance in the tracer experiments.

Assessment of body composition

Lean and fat mass body composition were analyzed using the EchoMRI-100H Analyzer (EchoMRI) according to the manufacturer's instructions (for detailed methods, see Supplementary Text).

Fasting-induced hyperphagic response

Feeding behavior was assessed with fasting-refeeding experiments. To this end, the afternoon before the test day, bedding material was changed, and mice were fasted overnight for 12 hours. At about 8:00 a.m., food was added, and its consumption was measured for the following 4 hours.

To assess glucose suppression of fasting-induced hyperphagia, mice were fasted overnight for 12 hours. The following day, mice were injected with either vehicle (0.9% saline) or glucose (2 g/kg body weight) intraperitoneally at 8:00 a.m., and food was provided 30 min after. Subsequently, food was weighted every hour for 4 hours to measure consumption.

In all cases, food intake was expressed as kcal (NCD = 2.7 kcal/g; HFD = 5.21 kcal/g), consumption corrected per animal body weight in grams (kcal/g BW).

Glucose and insulin metabolic tests

Glucose tolerance test

Sixteen- to 17-week-old mice were subjected to a fasting period of 6 hours. After the fasting period, a subtle puncture in the tail of each animal was performed, and a drop of tail blood was collected with a handheld glucometer (Accu-Chek) to measure fasting glucose levels (mg/dl). Then, mice received an intraperitoneal injection of D-glucose in 0.9% saline at a dose of 2 g/kg body weight. Blood glucose levels were measured by tail puncture at the following time points: 15, 30, 60, and 120 min after injection.

Insulin tolerance test

Sixteen- to 17-week-old mice were subjected to a fasting period of 1 hour, after which a subtle puncture in the tail of each animal was performed, and a drop of tail blood was collected with a handheld glucometer (Accu-Chek) to measure glucose levels. Then, they were intraperitoneally injected with insulin (Actrapid, Novo Nordisk) in 0.9% saline at a dose of 0.75 U/kg body weight. Glucose levels were measured at the following time points: 15, 30, and 60 min after injection.

Glucose-stimulated insulin secretion

Sixteen- to 17-week-old mice were subjected to a fasting period of 6 hours, after which a subtle puncture in the tail of each animal was performed, and a blood sample (minimum quantity: 12 μl of blood) was collected. Then, mice received an intravenous injection of D-glucose in 0.9% saline at a dose of 1 g/kg body weight. Blood samples (12 μl) were collected at the following time points: 2, 5, 15, and 30 min after injection. Blood glucose levels were measured at each time point using a handheld glucometer (Accu-Chek) to ensure that glucose levels first increased after injection and subsequently decreased. Mice that failed to increase blood glucose levels during the test were discarded. Blood samples were immediately centrifuged (10 min and 3500 rpm), and the resulting supernatant (serum) was collected and stored at −80°C until the determination of insulin levels.

Indirect calorimetry

Before treatment, animals were randomly selected and individually housed in chambers at 22° to 24°C with free access to food and water. After 48 hours of habituation to the chamber, the mice were housed for 5 days at 24°C. Oxygen consumption (VO_2) and carbon dioxide production (VCO_2) of individual mice were measured every 30 min over 5 days in LabMaster metabolic cages (TSE Systems). Energy expenditure was calculated with an abbreviated Weir equation, and respiratory exchange rate was calculated as VCO_2/VO_2.

Serum and CSF analyses

Serum insulin levels

Serum was collected as described above (see the "Glucose-stimulated insulin secretion" section). Insulin levels were assessed by enzyme-linked immunosorbent assay (ELISA) using the Ultra Sensitive Mouse Insulin ELISA (Crystal Chem, #90080) according to the manufacturer's instructions.

CSF glucose levels

Eighteen-week-old mice received an intraperitoneal injection containing either vehicle (0.9% saline) or glucose (2 g/kg body weight). After 30 min, mice were anesthetized using intraperitoneal ketamine/xylazine (80/5 mg/kg, respectively) and placed in a stereotaxic apparatus (David Kopf Instruments) to facilitate microdissection. Mice were carefully microdissected to expose the dura above the cisterna magna. CSF was collected from the cisterna magna by using a glass microcapillary. Once collected, samples were microscopically inspected to detect and discard blood-contaminated samples. Noncontaminated samples were immediately frozen and stored at −80°C until glucose determination. Glucose levels were assessed using the colorimetric Glucose Assay Kit (Abcam, #ab65333) according to the manufacturer's instructions.

Cold exposure

Core body temperature was measured in 18- to 20-week-old animals using a rectal probe attached to a digital thermometer (Panlab, Harvard Apparatus). Immediately after the first temperature measurement (−1 hour), mice were fasted, and a second measurement was performed 1 hour later (0 hour). Immediately, mice were placed into a 4°C room, in which they were kept for the following 4 hours. During this time, temperature was measured hourly.

Behavioral tasks

All behavioral experiments were carried out between 8 a.m. and 12 p.m. Researchers were blind to mice genotypes and treatments. All tests were undertaken in the same mice cohort at the age of 18 to 22 weeks.

Open field

To examine locomotor activity, mice were individually placed in a light-toned, wood-made open field (35 cm by 35 cm; height, 45 cm), being allowed to move freely for 30 min. The room was dimly illuminated, and a video-tracking system (EthoVision XT, Noldus Information Technology) was used to record all animal activity and to analyze the total distance traveled (in cm) for each mouse during the 30-min period.

Novel object recognition

The NOR task was used to test cognition and, particularly, to examine recognition memory, as previously described (for detailed methods, see Supplementary Text) (*73*, *74*).

Morris water maze

The MWM was used to test spatial memory and to evaluate the working and reference memory functions as previously described (for detailed methods, see Supplementary Text) (*55*).

AAV injection

AAV5-hGFAP-Cre–internal ribosomal entry site (IRES)–GFP injection in the ARC was performed following coordinates anteroposterior (AP), −1.5 mm; mediolateral (ML), ±0.3 mm; and dorsoventral (DV), −5.7 mm (for detailed methods, see Supplementary Text). For chemogenetic studies AAV8-GFAP-hM3D(Gq)-mCherry viral vector was injected at the coordinates from the bregma corresponding to the hippocampal CA1: AP, −2.1 mm; LM, ±1,6 mm; and DV, −1,5 mm (for detailed methods, see Supplementary Text).

Intracerebroventricular injections

Cannulation

Sixteen- to 17-week-old mice were subjected to brain cannulation (intralateral ventricular cannulation) with the following coordinates: AP, −0.4 mm; ML, +1.0 mm; and DV, −2 mm. Immediately, dental acrylic was applied to adhere the guide cannula to the skull surface (for detailed methods, see Supplementary Text).

Drug administration

For intracerebroventricular injections, a Hamilton syringe was used to administer 1 μl of 2 mM PPADS (Tocris), S961 (1.5 μg/μl; Phoenix Pharmaceuticals), or 20 μM 2-MeSATP (Tocris) over a 5-min period (for detailed methods, see Supplementary Text).

In vivo microdialysis

Eighteen-week-old mice were subjected to in vivo microdialysis. An intracerebral guide cannula (Microbiotech/se AB, #MAB 4.15.IC) was implanted to the frontal cortex using the following coordinates: AP, +2.0 mm; ML, +0.3 mm; and DV, −3.3 mm. Immediately, dental acrylic was applied to adhere the guide cannula to the skull surface. A dialysis probe with a cuprophane membrane (Microbiotech/se AB, #MAB 4.15.2.Cu) was inserted through the guide cannula, and animals were subjected to a stabilization period by being perfused with artificial CSF for 2 hours at a rate of 0.5 μl/min using a glass Hamilton syringe connected to an infusion pump. After the 2-hour stabilization period, samples started being collected every 30 min for 1 hour through a tube connected to the probe to measure basal ATP levels. After 1 hour of sample collection, mice were injected glucose intraperitoneally (2 g/kg body weight), and samples were collected every 30 min for another 1-hour period (for detailed methods, see Supplementary Text).

Cell sorting

Fluorescence-activated cell sorting

To isolate astrocytes from brains, a modified version of previously described protocols (*75, 76*) was followed (for detailed methods, see Supplementary Text).

Magnetic-activated cell sorting

To isolate astrocytes from brains, ensuring a gentle and not reactivity-triggering process for an accurate astrocyte reactivity gene profile analysis, MACS was performed (for detailed methods, see Supplementary Text).

Quantitative polymerase chain reaction

RNA extraction from cell samples was performed using the RNeasy Micro Kit (QIAGEN) or Maxwell RSC simplyRNA Tissue Kit (Promega) according to the manufacturer's instructions. RNA extraction from BAT samples was performed using the TRI Reagent (Sigma-Aldrich). Subsequently, RNA samples were subjected to retrotranscription using the High-Capacity cDNA Reverse Transcription Kit (Applied Biosystems). Quantitative real-time polymerase chain reaction (PCR) was performed on CFX384 Touch Real-Time PCR Detection System (Bio-Rad). TaqMan Universal PCR Master Mix (Applied Biosystems) was used with TaqMan Probes for *Gapdh*, *Insr*, *Slc2a1*, *Slc2a2*, *Slc2a3*, *Slc2a5*, and *Ucp1* (see table S1). iQ SYBR Green Supermix Reagent (Bio-Rad) was used with the SYBR probes detailed in the table S1. Sequences for the probes used to assess mRNA expression of the different transporters of the GLUT family were obtained from (*77*).

Sequences for the probes used to assess mRNA expression of astrocyte reactivity genes were obtained from (*78*). Relative quantification of the gene expression of all targets with respect to the control group was performed by a comparative method ($2^{-\Delta\Delta Ct}$). *Gapdh* was used as an internal control for all experiments except for the experiment assessing the mRNA expression of astrocyte reactivity genes where *Actb* was used as internal control.

Brain capillary depletion

To assess protein specifically in brain capillaries and in capillary-depleted brains, brain capillaries were separated using the previously described brain capillary depletion technique (*79–81*) with minor modifications (for detailed methods, see Supplementary Text).

Western blotting

The Western blotting studies following primary antibodies and dilutions were used: anti-GLUT1 (1:1000), anti-UCP1 (1:1000), anti-fibrinogen (1:1000), anti–ZO-1 (1:1000), anti-occludin (1:1000). β-Actin (1:5000) was used as internal loading control (for detailed methods and antibody catalog numbers, see Supplementary Text and table S1).

Histology

Pancreas and BAT immunohistochemistry

Mice faster for 6 hour were euthanized, and both BAT and pancreas were carefully dissected. BAT and pancreas were formalin fixed, paraffin embedded, and cut in 3-μm thick sections. Brown fat sections were stained with H&E for routine histology. In addition, immunohistochemistry was applied using the following primary antibodies: rabbit monoclonal anti-UCP1 (1:4000), rabbit monoclonal anti-insulin (1:80,000), and rabbit monoclonal anti-GFAP (1:200; for detailed methods and antibody catalog numbers, see Supplementary Text and table S1).

Brain slice immunofluorescence

Free-floating brain slices were stained with the following primary antibodies: anti-POMC (1:1000), anti-TH (1:1000), anti–c-Fos (1:500), anti-GFAP (1:1000), anti-GFP (1:1000), anti-NeuN (1:1000), anti-fibrin (1:1000), anti–ZO-1 (1:200), and anti-occludin (1:200). *Lycopersicon esculentum* lectin conjugated with fluorescein (1:200) was incubated together with the secondary antibody. All images were acquired using a confocal laser scanning microscope (LSM 800 with Airyscan, Zeiss) and the ZEN 2 Blue Edition software (Zeiss). For detailed methods and antibody catalog numbers, see Supplementary Text and table S1.

Astrocyte morphometric analysis

Imaging of astrocytes located in the stratum radiatum was performed using brain slice immunofluorescence of GFAP$^+$ cells and confocal laser scanning microscopy (see the "Brain slice immunofluorescence" section) with a 63× objective. Sholl analysis of astrocytic processes was performed semiautomatedly using Fiji, including the plugin "SNT" (https://imagej.net/plugins/snt), as described previously (for detailed methods, see Supplementary Text) (*82*).

Dendritic spine density analysis

Golgi-Cox staining and image acquisition

For dendritic spine density analysis, the FD Rapid GolgiStain Kit (FD Neuro Technologies) was used according to the manufacturer's instructions (for detailed methods, see Supplementary Text).

Dendritic spine quantification

Dendritic spines were analyzed using the Reconstruct software (*83*), as previously described (for detailed methods, see Supplementary Text) (*84*).

Whole-brain clearing and three-dimensional blood vessel analysis

Vessel staining of cleared mouse brain slices

Mice were transcardially perfused with phosphate-buffered saline (PBS; pH 7.4) and 10 ml of 4% paraformaldehyde in PBS. Brains were dissected and then postfixed with 4% paraformaldehyde overnight. Then, 500-μm-thick brain slices were sectioned using a vibratome (VT1000S, Leica) and maintained in PBS solution at 4°C for tissue clearing. Sections were cleared following the CUBIC protocol (for detailed methods, see Supplementary Text) (*85*).

Two-photon excitation microscopy

Images were collected using a Zeiss LSM 880 (Carl Zeiss, Jena, Germany) equipped with a two-photon femtosecond pulsed laser (Mai Tai DeepSee, Spectra-Physics, USA), tuned to a central wavelength of 800 nm using a 25× objective (LD LCI Plan-Apochromat 25x/0.8, Carl Zeiss). Tile and *z*-stack scans from 500-μm sections were acquired in the non-descanned mode after spectral separation and emission refiltering using a 500- to 550-nm BP filter for lectin signal.

Vessel image analysis

Vessel quantification in fluorescent three-dimensional (3D) image stacks was carried out using an automatized homemade Fiji plugin. First, 3D images were preprocessed by means of a background subtraction operation followed by a tubeness filter (*86*) to enhance tube-like structures. Then, vessels were segmented by thresholding the image using a constant threshold value across all images. The resulting binary mask was further refined by means of a median filter and small particle removal, and the total vessel volume (in μm^3) and vessel density (as percentage of tissue occupied by vessels) were calculated. The segmentation mask was lastly skeletonized in 3D, and the resulting skeleton was analyzed (*87*) to quantify the number of vessels, the average vessel length (in μm), and the normalized vessel length (in m/mm^3).

Metabolomic studies

High-resolution magic angle spinning (HR-MAS) ^1H NMR spectroscopy permits the direct analysis of intact tissues to obtain highly resolved spectra. Because the technique requires only small amounts of tissue (typically 5 to 20 mg), it is possible to define the biochemical profile for localized regions in heterogeneous tissues such as the brain. In this study, multivariate statistical algorithms were used to classify HR-MAS ^1H NMR spectra of the hippocampus and hypothalamus and identify distinct metabolic profiles for these tissues.

NMR data acquisition

Hippocampal and hypothalamus samples were examined using HR-MAS operating at 4°C to minimize tissue degradation. ^1H-NMR spectroscopy was performed in the ICTS Bioimagen Complutense (Universidad Complutense, Madrid, Spain) at 500.13 MHz using a Bruker AVIII500 HD spectrometer (11.7 T) (for detailed methods, see Supplementary Text).

2D experiment

^1H, ^{13}C 2D experiments were performed to carry out the components assignments (for detailed methods, see Supplementary Text).

Pattern recognition

In this study, multivariate statistical algorithms were used to classify HR-MAS ^1H NMR spectra of these samples and identify distinct metabolic profiles for the tissues (for detailed methods, see Supplementary Text).

Proteomic analysis

For detailed methods of protein extraction, MS/MS library generation, quantitative analysis, and weighted protein coexpression network analysis, see Supplementary Text.

Statistical analysis

All values were expressed as means ± SEM. Statistical analyses were conducted using GraphPad Prism (version 9.3.1). Statistical details of experiments can be found in the figure legends. Unless otherwise specified in the figure legends, datasets with only two independent groups were analyzed for statistical significance using unpaired, two-tailed Student's *t* test. Datasets with more than two groups were analyzed using one-way analysis of variance (ANOVA), followed by Tukey post hoc test. Datasets with two independent factors were analyzed using two-way ANOVA, followed by Tukey post hoc test. Two-way repeated-measures ANOVA was performed to detect significant interactions between genotype and time, and multiple comparisons were analyzed following Tukey's post hoc tests. All *P* values below or equal to 0.05 were considered significant ($*P \leq 0.05$, $**P \leq 0.01$, and $***P \leq 0.001$).

Supplementary Materials

This PDF file includes:

Supplementary Text
Figs. S1 to S9
Tables S1
Unprocessed Original Blots
References

REFERENCES AND NOTES

1. M. Bélanger, I. Allaman, P. J. Magistretti, Brain energy metabolism: Focus on astrocyte-neuron metabolic cooperation. *Cell Metab.* **14**, 724–738 (2011).
2. J. W. Mink, R. J. Blumenschine, D. B. Adams, Ratio of central nervous system to body metabolism in vertebrates: its constancy and functional basis. *Am. J. Physiol.* **241**, R203–R212 (1981).
3. M. C. McKenna, R. Gruetter, U. Sonnewald, H. S. Waagepetersen, A. Schousboe, "Energy metabolism of the brain" in *Basic Neurochemistry: Molecular, Cellular and Medical Aspects*, G. J. Siegel, R. W. Alberts, S. T. Brady, D. L. Price, Eds. (Elsevier Academic Press, Burlington, MA, ed. 7, 2006), pp. 531–557.
4. E. L. Roberts, "The support of energy metabolism in the central nervous system with substrates other than glucose" in *Handbook of Neurochemistry and Molecular Neurobiology: Brain Energetics. Integration of Molecular and Cellular Processes*, A. Lajtha, G. E. Gibson, G. A. Dienel, Eds. (Springer, 2007), pp. 137–179; https://doi.org/10.1007/978-0-387-30411-3_7.
5. J. Pearson-Leary, E. C. McNay, Novel roles for the insulin-regulated glucose transporter-4 in hippocampally dependent memory. *J. Neurosci.* **36**, 11851–11864 (2016).
6. J. Pearson-Leary, V. Jahagirdar, J. Sage, E. C. McNay, Insulin modulates hippocampally-mediated spatial working memory via glucose transporter-4. *Behav. Brain Res.* **338**, 32–39 (2018).
7. E. Roh, D. K. Song, M.-S. Kim, Emerging role of the brain in the homeostatic regulation of energy and glucose metabolism. *Exp. Mol. Med.* **48**, e216 (2016).
8. K. Timper, J. C. Brüning, Hypothalamic circuits regulating appetite and energy homeostasis: Pathways to obesity. *Dis. Model. Mech.* **10**, 679–689 (2017).

9. S. J. Vannucci, F. Maher, I. A. Simpson, Glucose transporter proteins in brain: Delivery of glucose to neurons and glia. *Glia* **21**, 2–21 (1997).
10. Y. Zhang, K. Chen, S. A. Sloan, M. L. Bennett, A. R. Scholze, S. O'Keeffe, H. P. Phatnani, P. Guarnieri, C. Caneda, N. Ruderisch, S. Deng, S. A. Liddelow, C. Zhang, R. Daneman, T. Maniatis, B. A. Barres, J. Q. Wu, An RNA-sequencing transcriptome and splicing database of glia, neurons, and vascular cells of the cerebral cortex. *J. Neurosci.* **34**, 11929–11947 (2014).
11. K. Kacem, P. Lacombe, J. Seylaz, G. Bonvento, Structural organization of the perivascular astrocyte endfeet and their relationship with the endothelial glucose transporter: A confocal microscopy study. *Glia* **23**, 1–10 (1998).
12. G. Ashrafi, Z. Wu, R. J. Farrell, T. A. Ryan, GLUT4 mobilization supports energetic demands of active synapses. *Neuron* **93**, 606–615.e3 (2017).
13. I. A. Simpson, A. Carruthers, S. J. Vannucci, Supply and demand in cerebral energy metabolism: The role of nutrient transporters. *J. Cereb. Blood Flow Metab.* **27**, 1766–1791 (2007).
14. L. Pellerin, P. J. Magistretti, Glutamate uptake into astrocytes stimulates aerobic glycolysis: A mechanism coupling neuronal activity to glucose utilization. *Proc. Natl. Acad. Sci. U.S.A.* **91**, 10625–10629 (1994).
15. P. Mächler, M. T. Wyss, M. Elsayed, J. Stobart, R. Gutierrez, A. von Faber-Castell, V. Kaelin, M. Zuend, A. San Martín, I. Romero-Gómez, F. Baeza-Lehnert, S. Lengacher, B. L. Schneider, P. Aebischer, P. J. Magistretti, L. F. Barros, B. Weber, In vivo evidence for a lactate gradient from astrocytes to neurons. *Cell Metab.* **23**, 94–102 (2016).
16. M. Zuend, A. S. Saab, M. T. Wyss, K. D. Ferrari, L. Hösli, Z. J. Looser, J. L. Stobart, J. Duran, J. J. Guinovart, L. F. Barros, B. Weber, Arousal-induced cortical activity triggers lactate release from astrocytes. *Nat. Metab.* **2**, 179–191 (2020).
17. L. K. Bak, A. B. Walls, CrossTalk opposing view: Lack of evidence supporting an astrocyte-to-neuron lactate shuttle coupling neuronal activity to glucose utilisation in the brain. *J. Physiol.* **596**, 351–353 (2018).
18. L. F. Barros, B. Weber, CrossTalk proposal: An important astrocyte-to-neuron lactate shuttle couples neuronal activity to glucose utilisation in the brain. *J. Physiol.* **596**, 347–350 (2018).
19. F. Baeza-Lehnert, A. S. Saab, R. Gutiérrez, V. Larenas, E. Díaz, M. Horn, M. Vargas, L. Hösli, J. Stobart, J. Hirrlinger, B. Weber, L. F. Barros, Non-canonical control of neuronal energy status by the Na^+ pump. *Cell Metab.* **29**, 668–680.e4 (2019).
20. C. M. Díaz-García, R. Mongeon, C. Lahmann, D. Koveal, H. Zucker, G. Yellen, Neuronal stimulation triggers neuronal glycolysis and not lactate uptake. *Cell Metab.* **26**, 361–374.e4 (2017).
21. J.-O. Hollnagel, T. Cesetti, J. Schneider, A. Vazetdinova, F. Valiullina-Rakhmatullina, A. Lewen, A. Rozov, O. Kann, Lactate attenuates synaptic transmission and affects brain rhythms featuring high energy expenditure. *iScience* **23**, 101316 (2020).
22. L. V. Galow, J. Schneider, A. Lewen, T.-T. Ta, I. E. Papageorgiou, O. Kann, Energy substrates that fuel fast neuronal network oscillations. *Front. Neurosci.* **8**, 398 (2014).
23. B. Morant-Ferrando, D. Jimenez-Blasco, P. Alonso-Batan, J. Agulla, R. Lapresa, D. Garcia-Rodriguez, S. Yunta-Sanchez, I. Lopez-Fabuel, E. Fernandez, P. Carmeliet, A. Almeida, M. Garcia-Macia, J. P. Bolaños, Fatty acid oxidation organizes mitochondrial supercomplexes to sustain astrocytic ROS and cognition. *Nat. Metab.* **5**, 1290–1302 (2023).
24. K. Timper, A. Del Río-Martín, A. L. Cremer, S. Bremser, J. Alber, P. Giavalisco, L. Varela, C. Heilinger, H. Nolte, A. Trifunovic, T. L. Horvath, P. Kloppenburg, H. Backes, J. C. Brüning, GLP-1 receptor signaling in astrocytes regulates fatty acid oxidation, mitochondrial integrity, and function. *Cell Metab.* **31**, 1189–1205.e13 (2020).
25. C. García-Cáceres, C. Quarta, L. Varela, Y. Gao, T. Gruber, B. Legutko, M. Jastroch, P. Johansson, J. Ninkovic, C.-X. Yi, O. Le Thuc, K. Szigeti-Buck, W. Cai, C. W. Meyer, P. T. Pfluger, A. M. Fernandez, S. Luquet, S. C. Woods, I. Torres-Alemán, C. R. Kahn, M. Götz, T. L. Horvath, M. H. Tschöp, Astrocytic insulin signaling couples brain glucose uptake with nutrient availability. *Cell* **166**, 867–880 (2016).
26. N. Chen, H. Sugihara, J. Kim, Z. Fu, B. Barak, M. Sur, G. Feng, W. Han, Direct modulation of GFAP-expressing glia in the arcuate nucleus bi-directionally regulates feeding. *eLife* **5**, e18716 (2016).
27. Y. Gao, C. Layritz, B. Legutko, T. O. Eichmann, E. Laperrousaz, V. S. Moullé, C. Cruciani-Guglielmacci, C. Magnan, S. Luquet, S. C. Woods, R. H. Eckel, C.-X. Yi, C. Garcia-Caceres, M. H. Tschöp, Disruption of lipid uptake in astroglia exacerbates diet-induced obesity. *Diabetes* **66**, 2555–2563 (2017).
28. L. Yang, Y. Qi, Y. Yang, Astrocytes control food intake by inhibiting AGRP neuron activity via adenosine A_1 receptors. *Cell Rep.* **11**, 798–807 (2015).
29. Y. Zhang, J. M. Reichel, C. Han, J. P. Zuniga-Hertz, D. Cai, Astrocytic process plasticity and IKKβ/NF-κB in central control of blood glucose, blood pressure, and body weight. *Cell Metab.* **25**, 1091–1102.e4 (2017).
30. A. Adamsky, A. Kol, T. Kreisel, A. Doron, N. Ozeri-Engelhard, T. Melcer, R. Refaeli, H. Horn, L. Regev, M. Groysman, M. London, I. Goshen, Astrocytic activation generates *de novo* neuronal potentiation and memory enhancement. *Cell* **174**, 59–71.e14 (2018).
31. A. Kol, A. Adamsky, M. Groysman, T. Kreisel, M. London, I. Goshen, Astrocytes contribute to remote memory formation by modulating hippocampal-cortical communication during learning. *Nat. Neurosci.* **23**, 1229–1239 (2020).
32. A. Pinto-Duarte, A. J. Roberts, K. Ouyang, T. J. Sejnowski, Impairments in remote memory caused by the lack of type 2 IP_3 receptors. *Glia* **67**, 1976–1989 (2019).
33. A. Suzuki, S. A. Stern, O. Bozdagi, G. W. Huntley, R. H. Walker, P. J. Magistretti, C. M. Alberini, Astrocyte-neuron lactate transport is required for long-term memory formation. *Cell* **144**, 810–823 (2011).
34. E. A. Winkler, Y. Nishida, A. P. Sagare, S. V. Rege, R. D. Bell, D. Perlmutter, J. D. Sengillo, S. Hillman, P. Kong, A. R. Nelson, J. S. Sullivan, Z. Zhao, H. J. Meiselman, R. B. Wendy, J. Soto, E. D. Abel, J. Makshanoff, E. Zuniga, D. C. De Vivo, B. V. Zlokovic, GLUT1 reductions exacerbate Alzheimer's disease vasculo-neuronal dysfunction and degeneration. *Nat. Neurosci.* **18**, 521–530 (2015).
35. D. Cota, K. Proulx, R. J. Seeley, The role of CNS fuel sensing in energy and glucose regulation. *Gastroenterology* **132**, 2158–2168 (2007).
36. G. T. Dodd, N. J. Michael, R. S. Lee-Young, S. P. Mangiafico, J. T. Pryor, A. C. Munder, S. E. Simonds, J. C. Brüning, Z.-Y. Zhang, M. A. Cowley, S. Andrikopoulos, T. L. Horvath, D. Spanswick, T. Tiganis, Insulin regulates POMC neuronal plasticity to control glucose metabolism. *eLife* **7**, e38704 (2018).
37. M. J. Krashes, B. B. Lowell, A. S. Garfield, Melanocortin-4 receptor–regulated energy homeostasis. *Nat. Neurosci.* **19**, 206–219 (2016).
38. S. Ramírez, A. G. Gómez-Valadés, M. Schneeberger, L. Varela, R. Haddad-Tóvolli, J. Altirriba, E. Noguera, A. Drougard, Á. Flores-Martínez, M. Imbernón, I. Chivite, M. Pozo, A. Vidal-Itriago, A. Garcia, S. Cervantes, R. Gasa, R. Nogueiras, P. Gama-Pérez, P. M. Garcia-Roves, D. A. Cano, C. Knauf, J.-M. Servitja, T. L. Horvath, R. Gomis, A. Zorzano, M. Claret, Mitochondrial dynamics mediated by mitofusin 1 is required for POMC neuron glucose-sensing and insulin release control. *Cell Metab.* **25**, 1390–1399.e6 (2017).
39. E. Fuente-Martín, C. García-Cáceres, M. Granado, M. L. de Ceballos, M. Á. Sánchez-Garrido, B. Sarman, Z.-W. Liu, M. O. Dietrich, M. Tena-Sempere, P. Argente-Arizón, F. Díaz, J. Argente, T. L. Horvath, J. A. Chowen, Leptin regulates glutamate and glucose transporters in hypothalamic astrocytes. *J. Clin. Invest.* **122**, 3900–3913 (2012).
40. S. Tovar, L. Paeger, S. Hess, D. A. Morgan, A. C. Hausen, H. S. Brönneke, B. Hampel, P. J. Ackermann, N. Evers, H. Büning, F. T. Wunderlich, K. Rahmouni, P. Kloppenburg, J. C. Brüning, K_{ATP}-channel-dependent regulation of catecholaminergic neurons controls BAT SYmpathetic nerve activity and energy homeostasis. *Cell Metab.* **18**, 445–455 (2013).
41. M. V. Sofroniew, H. V. Vinters, Astrocytes: Biology and pathology. *Acta Neuropathol.* **119**, 7–35 (2010).
42. L. Mosconi, R. Mistur, R. Switalski, W. H. Tsui, L. Glodzik, Y. Li, E. Pirraglia, S. De Santi, B. Reisberg, T. Wisniewski, M. J. de Leon, FDG-PET changes in brain glucose metabolism from normal cognition to pathologically verified Alzheimer's disease. *Eur. J. Nucl. Med. Mol. Imaging* **36**, 811–822 (2009).
43. H. D. Protas, K. Chen, J. B. S. Langbaum, A. S. Fleisher, G. E. Alexander, W. Lee, D. Bandy, M. J. de Leon, L. Mosconi, S. Buckley, D. Truran-Sacrey, N. Schuff, M. W. Weiner, R. J. Caselli, E. M. Reiman, Posterior cingulate glucose metabolism, hippocampal glucose metabolism, and hippocampal volume in cognitively normal, late-middle-aged persons at 3 levels of genetic risk for Alzheimer disease. *JAMA Neurol.* **70**, 320–325 (2013).
44. A. Doron, A. Rubin, A. Benmelech-Chovav, N. Benaim, T. Carmi, R. Refaeli, N. Novick, T. Kreisel, Y. Ziv, I. Goshen, Hippocampal astrocytes encode reward location. *Nature* **609**, 772–778 (2022).
45. M. A. Di Castro, J. Chuquet, N. Liaudet, K. Bhaukaurally, M. Santello, D. Bouvier, P. Tiret, A. Volterra, Local Ca^{2+} detection and modulation of synaptic release by astrocytes. *Nat. Neurosci.* **14**, 1276–1284 (2011).
46. P. Jourdain, L. H. Bergersen, K. Bhaukaurally, P. Bezzi, M. Santello, M. Domercq, C. Matute, F. Tonello, V. Gundersen, A. Volterra, Glutamate exocytosis from astrocytes controls synaptic strength. *Nat. Neurosci.* **10**, 331–339 (2007).
47. X. Cao, L.-P. Li, Q. Wang, Q. Wu, H.-H. Hu, M. Zhang, Y.-Y. Fang, J. Zhang, S.-J. Li, W.-C. Xiong, H.-C. Yan, Y.-B. Gao, J.-H. Liu, X.-W. Li, L.-R. Sun, Y.-N. Zeng, X.-H. Zhu, T.-M. Gao, Astrocyte-derived ATP modulates depressive-like behaviors. *Nat. Med.* **19**, 773–777 (2013).
48. W. Cai, C. Xue, M. Sakaguchi, M. Konishi, A. Shirazian, H. A. Ferris, M. E. Li, R. Yu, A. Kleinridders, E. N. Pothos, C. R. Kahn, Insulin regulates astrocyte gliotransmission and modulates behavior. *J. Clin. Invest.* **128**, 2914–2926 (2018).
49. A. Araque, G. Carmignoto, P. G. Haydon, S. H. R. Oliet, R. Robitaille, A. Volterra, Gliotransmitters travel in time and space. *Neuron* **81**, 728–739 (2014).
50. M. Soto, W. Cai, M. Konishi, C. R. Kahn, Insulin signaling in the hippocampus and amygdala regulates metabolism and neurobehavior. *Proc. Natl. Acad. Sci. U.S.A.* **116**, 6379–6384 (2019).
51. W. Chen, Q. Huang, E. K. Lazdon, A. Gomes, M. Wong, E. Stephens, T. G. Royal, D. Frenkel, W. Cai, C. R. Kahn, Loss of insulin signaling in astrocytes exacerbates Alzheimer-like phenotypes in a 5xFAD mouse model. *Proc. Natl. Acad. Sci. U.S.A.* **120**, e2220684120 (2023).
52. G. J. Biessels, L. P. Reagan, Hippocampal insulin resistance and cognitive dysfunction. *Nat. Rev. Neurosci.* **16**, 660–671 (2015).

53. F. G. De Felice, R. A. Gonçalves, S. T. Ferreira, Impaired insulin signalling and allostatic load in Alzheimer disease. *Nat. Rev. Neurosci.* **23**, 215–230 (2022).
54. S. M. Steculorum, M. Solas, J. C. Brüning, The paradox of neuronal insulin action and resistance in the development of aging-associated diseases. *Alzheimers Dement.* **10**, S3–S11 (2014).
55. A. Jais, M. Solas, H. Backes, B. Chaurasia, A. Kleinridders, S. Theurich, J. Mauer, S. M. Steculorum, B. Hampel, J. Goldau, J. Alber, C. Y. Förster, S. A. Eming, M. Schwaninger, N. Ferrara, G. Karsenty, J. C. Brüning, Myeloid-cell-derived VEGF maintains brain glucose uptake and limits cognitive impairment in obesity. *Cell* **165**, 882–895 (2016).
56. K. Veys, Z. Fan, M. Ghobrial, A. Bouché, M. García-Caballero, K. Vriens, N. V. Conchinha, A. Seuwen, F. Schlegel, T. Gorski, M. Crabbé, P. Gilardoni, R. Ardicoglu, J. Schaffenrath, C. Casteels, G. De Smet, I. Smolders, K. Van Laere, E. D. Abel, S.-M. Fendt, A. Schroeter, J. Kalucka, A. R. Cantelmo, T. Wälchli, A. Keller, P. Carmeliet, K. De Bock, Role of the GLUT1 glucose transporter in postnatal CNS angiogenesis and blood-brain barrier integrity. *Circ. Res.* **127**, 466–482 (2020).
57. T. M. Mathiisen, K. P. Lehre, N. C. Danbolt, O. P. Ottersen, The perivascular astroglial sheath provides a complete covering of the brain microvessels: An electron microscopic 3D reconstruction. *Glia* **58**, 1094–1103 (2010).
58. L. Hösli, M. Zuend, G. Bredell, H. S. Zanker, C. E. Porto de Oliveira, A. S. Saab, B. Weber, Direct vascular contact is a hallmark of cerebral astrocytes. *Cell Rep.* **39**, 110599 (2022).
59. A. Herrero-Mendez, A. Almeida, E. Fernández, C. Maestre, S. Moncada, J. P. Bolaños, The bioenergetic and antioxidant status of neurons is controlled by continuous degradation of a key glycolytic enzyme by APC/C–Cdh1. *Nat. Cell Biol.* **11**, 747–752 (2009).
60. D. Jimenez-Blasco, J. Agulla, R. Lapresa, M. Garcia-Macia, V. Bobo-Jimenez, D. Garcia-Rodriguez, I. Manjarres-Raza, E. Fernandez, Y. Jeanson, S. Khoury, J.-C. Portais, D. Padro, P. Ramos-Cabrer, P. Carmeliet, A. Almeida, J. P. Bolaños, Weak neuronal glycolysis sustains cognition and organismal fitness. *Nat. Metab.* **6**, 1253–1267 (2024).
61. J. Cheng, R. Zhang, Z. Xu, Y. Ke, R. Sun, H. Yang, X. Zhang, X. Zhen, L.-T. Zheng, Early glycolytic reprogramming controls microglial inflammatory activation. *J. Neuroinflammation* **18**, 129 (2021).
62. R. Holland, A. L. McIntosh, O. M. Finucane, V. Mela, A. Rubio-Araiz, G. Timmons, S. A. McCarthy, Y. K. Gun'ko, M. A. Lynch, Inflammatory microglia are glycolytic and iron retentive and typify the microglia in APP/PS1 mice. *Brain Behav. Immun.* **68**, 183–196 (2018).
63. S. Yang, C. Qin, Z.-W. Hu, L.-Q. Zhou, H.-H. Yu, M. Chen, D. B. Bosco, W. Wang, L.-J. Wu, D.-S. Tian, Microglia reprogram metabolic profiles for phenotype and function changes in central nervous system. *Neurobiol. Dis.* **152**, 105290 (2021).
64. X. Xiang, K. Wind, T. Wiedemann, T. Blume, Y. Shi, N. Briel, L. Beyer, G. Biechele, F. Eckenweber, A. Zatcepin, S. Lammich, S. Ribicic, S. Tahirovic, M. Willem, M. Deussing, C. Palleis, B.-S. Rauchmann, F.-J. Gildehaus, S. Lindner, C. Spitz, N. Franzmeier, K. Baumann, A. Rominger, P. Bartenstein, S. Ziegler, A. Drzezga, G. Respondek, K. Buerger, R. Perneczky, J. Levin, G. U. Höglinger, J. Herms, C. Haass, M. Brendel, Microglial activation states drive glucose uptake and FDG-PET alterations in neurodegenerative diseases. *Sci. Transl. Med.* **13**, eabe5640 (2021).
65. U. Fünfschilling, L. M. Supplie, D. Mahad, S. Boretius, A. S. Saab, J. Edgar, B. G. Brinkmann, C. M. Kassmann, I. D. Tzvetanova, W. Möbius, F. Diaz, D. Meijer, U. Suter, B. Hamprecht, M. W. Sereda, C. T. Moraes, J. Frahm, S. Goebbels, K.-A. Nave, Glycolytic oligodendrocytes maintain myelin and long-term axonal integrity. *Nature* **485**, 517–521 (2012).
66. A. S. Saab, I. D. Tzvetavona, A. Trevisiol, S. Baltan, P. Dibaj, K. Kusch, W. Möbius, B. Goetze, H. M. Jahn, W. Huang, H. Steffens, E. D. Schomburg, A. Pérez-Samartín, F. Pérez-Cerdá, D. Bakhtiari, C. Matute, S. Löwel, C. Griesinger, J. Hirrlinger, F. Kirchhoff, K.-A. Nave, Oligodendroglial NMDA receptors regulate glucose import and axonal energy metabolism. *Neuron* **91**, 119–132 (2016).
67. C. Quarta, M. Claret, L. M. Zeltser, K. W. Williams, G. S. H. Yeo, M. H. Tschöp, S. Diano, J. C. Brüning, D. Cota, POMC neuronal heterogeneity in energy balance and beyond: An integrated view. *Nat. Metab.* **3**, 299–308 (2021).
68. L. E. Parton, C. P. Ye, R. Coppari, P. J. Enriori, B. Choi, C.-Y. Zhang, C. Xu, C. R. Vianna, N. Balthasar, C. E. Lee, J. K. Elmquist, M. A. Cowley, B. B. Lowell, Glucose sensing by POMC neurons regulates glucose homeostasis and is impaired in obesity. *Nature* **449**, 228–232 (2007).
69. L. Crosby, B. Davis, S. Joshi, M. Jardine, J. Paul, M. Neola, N. D. Barnard, Ketogenic diets and chronic disease: Weighing the benefits against the risks. *Front. Nutr.* **8**, 702802 (2021).
70. J. Wei, J. Shimazu, M. P. Makinistoglu, A. Maurizi, D. Kajimura, H. Zong, T. Takarada, T. Iezaki, J. E. Pessin, E. Hinoi, G. Karsenty, Glucose uptake and Runx2 synergize to orchestrate osteoblast differentiation and bone formation. *Cell* **161**, 1576–1591 (2015).
71. J. C. Brüning, M. D. Michael, J. N. Winnay, T. Hayashi, D. Hörsch, D. Accili, L. J. Goodyear, C. R. Kahn, A muscle-specific insulin receptor knockout exhibits features of the metabolic syndrome of NIDDM without altering glucose tolerance. *Mol. Cell* **2**, 559–569 (1998).
72. Y. M. Ganat, J. Silbereis, C. Cave, H. Ngu, G. M. Anderson, Y. Ohkubo, L. R. Ment, F. M. Vaccarino, Early postnatal astroglial cells produce multilineage precursors and neural stem cells in vivo. *J. Neurosci.* **26**, 8609–8621 (2006).
73. M. Leger, A. Quiedeville, V. Bouet, B. Haelewyn, M. Boulouard, P. Schumann-Bard, T. Freret, Object recognition test in mice. *Nat. Protoc.* **8**, 2531–2537 (2013).
74. L. M. Lueptow, Novel object recognition test for the investigation of learning and memory in mice. *J. Vis. Exp.* , 55718 (2017).
75. O. Abiega, S. Beccari, I. Diaz-Aparicio, A. Nadjar, S. Layé, Q. Leyrolle, D. Gómez-Nicola, M. Domercq, A. Pérez-Samartín, V. Sánchez-Zafra, I. Paris, J. Valero, J. C. Savage, C.-W. Hui, M.-È. Tremblay, J. J. P. Deudero, A. L. Brewster, A. E. Anderson, L. Zaldumbide, L. Galbarriatu, A. Marinas, M. dM Vivanco, C. Matute, M. Maletic-Savatic, J. M. Encinas, A. Sierra, Neuronal hyperactivity disturbs ATP microgradients, impairs microglial motility, and reduces phagocytic receptor expression triggering apoptosis/microglial phagocytosis uncoupling. *PLOS Biol.* **14**, e1002466 (2016).
76. I. Diaz-Aparicio, I. Paris, V. Sierra-Torre, A. Plaza-Zabala, N. Rodríguez-Iglesias, M. Márquez-Ropero, S. Beccari, P. Huguet, O. Abiega, E. Alberdi, C. Matute, I. Bernales, A. Schulz, L. Otrokocsi, B. Sperlagh, K. E. Happonen, G. Lemke, M. Maletic-Savatic, J. Valero, A. Sierra, Microglia actively remodel adult hippocampal neurogenesis through the phagocytosis secretome. *J. Neurosci.* **40**, 1453–1482 (2020).
77. S.-Y. Lee, H.-S. Lee, E.-Y. Kim, J.-J. Ko, T. K. Yoon, W.-S. Lee, K.-A. Lee, Thioredoxin-interacting protein regulates glucose metabolism and affects cytoplasmic streaming in mouse oocytes. *PLOS One* **8**, e70708 (2013).
78. S. A. Liddelow, K. A. Guttenplan, L. E. Clarke, F. C. Bennett, C. J. Bohlen, L. Schirmer, M. L. Bennett, A. E. Münch, W.-S. Chung, T. C. Peterson, D. K. Wilton, A. Frouin, B. A. Napier, N. Panicker, M. Kumar, M. S. Buckwalter, D. H. Rowitch, V. L. Dawson, T. M. Dawson, B. Stevens, B. A. Barres, Neurotoxic reactive astrocytes are induced by activated microglia. *Nature* **541**, 481–487 (2017).
79. K. B. Johnsen, A. Burkhart, F. Melander, P. J. Kempen, J. B. Vejlebo, P. Siupka, M. S. Nielsen, T. L. Andresen, T. Moos, Targeting transferrin receptors at the blood-brain barrier improves the uptake of immunoliposomes and subsequent cargo transport into the brain parenchyma. *Sci. Rep.* **7**, 10396 (2017).
80. I. Singh, A. P. Sagare, M. Coma, D. Perlmutter, R. Gelein, R. D. Bell, R. J. Deane, E. Zhong, M. Parisi, J. Ciszewski, R. T. Kasper, R. Deane, Low levels of copper disrupt brain amyloid-β homeostasis by altering its production and clearance. *Proc. Natl. Acad. Sci. U.S.A.* **110**, 14771–14776 (2013).
81. D. Triguero, J. Buciak, W. M. Pardridge, Capillary depletion method for quantification of blood–brain barrier transport of circulating peptides and plasma proteins. *J. Neurochem.* **54**, 1882–1888 (1990).
82. G. Tavares, M. Martins, J. S. Correia, V. M. Sardinha, S. Guerra-Gomes, S. P. das Neves, F. Marques, N. Sousa, J. F. Oliveira, Employing an open-source tool to assess astrocyte tridimensional structure. *Brain Struct. Funct.* **222**, 1989–1999 (2017).
83. J. C. Fiala, Reconstruct: A free editor for serial section microscopy. *J. Microsc.* **218**, 52–61 (2005).
84. W. C. Risher, T. Ustunkaya, J. S. Alvarado, C. Eroglu, Rapid Golgi analysis method for efficient and unbiased classification of dendritic spines. *PLOS One* **9**, e107591 (2014).
85. E. A. Susaki, K. Tainaka, D. Perrin, H. Yukinaga, A. Kuno, H. R. Ueda, Advanced CUBIC protocols for whole-brain and whole-body clearing and imaging. *Nat. Protoc.* **10**, 1709–1727 (2015).
86. Y. Sato, S. Nakajima, N. Shiraga, H. Atsumi, S. Yoshida, T. Koller, G. Gerig, R. Kikinis, Three-dimensional multi-scale line filter for segmentation and visualization of curvilinear structures in medical images. *Med. Image Anal.* **2**, 143–168 (1998).
87. I. Arganda-Carreras, R. Fernández-González, A. Muñoz-Barrutia, C. Ortiz-De-Solorzano, 3D reconstruction of histological sections: Application to mammary gland tissue. *Microsc. Res. Tech.* **73**, 1019–1029 (2010).
88. K. D. McCarthy, J. de Vellis, 3D reconstruction of histological sections: Application to mammary gland tissue. *Microsc. Res. Tech.* **85**, 890–902 (2010).
89. J. Votteler, C. Ogohara, S. Yi, Y. Hsia, U. Nattermann, D. M. Belnap, N. P. King, W. I. Sundquist, Designed proteins induce the formation of nanocage-containing extracellular vesicles. *Nature* **540**, 292–295 (2016).
90. J. Schindelin, I. Arganda-Carreras, E. Frise, V. Kaynig, M. Longair, T. Pietzsch, S. Preibisch, C. Rueden, S. Saalfeld, B. Schmid, J.-Y. Tinevez, D. J. White, V. Hartenstein, K. Eliceiri, P. Tomancak, A. Cardona, Fiji: an open-source platform for biological-image analysis. *Nat. Methods* **9**, 676–682 (2012).
91. W. H. Tang, I. V. Shilov, S. L. Seymour, , Nonlinear fitting method for determining local false discovery rates from decoy database searches.. *J. Proteome Res.* **7**, 3661–3667 (2008).
92. L. C. Gillet, P. Navarro, S. Tate, H. Röst, N. Selevsek, L. Reiter, R. Bonner, R. Aebersold, Targeted data extraction of the MS/MS spectra generated by data-independent acquisition: a new concept for consistent and accurate proteome analysis. *Mol. Cell. Proteomics MCP* **11**, O111.016717 (2012).
93. S. Okuda, Y. Watanabe, Y. Moriya, S. Kawano, T. Yamamoto, M. Matsumoto, T. Takami, D. Kobayashi, N. Araki, A. C. Yoshizawa, T. Tabata, N. Sugiyama, S. Goto, Y. Ishihama, jPOSTrepo: an international standard data repository for proteomes. *Nucleic Acids Res.* **45**, D1107–D1111 (2017).
94. P. Langfelder, S. Horvath, WGCNA: an R package for weighted correlation network analysis. *BMC Bioinformatics* **9**, 559 (2008).
95. B. Zhang, S. Horvath, A general framework for weighted gene co-expression network analysis. *Stat. Appl. Genet. Mol. Biol.* **4**, Article17 (2005).

96. S. X. Ge, D. Jung, R. Yao, ShinyGO: a graphical gene-set enrichment tool for animals and plants. *Bioinforma. Oxf. Engl.* **36**, 2628–2629 (2020).

Acknowledgments: We acknowledge all JPOST Team for helping with the mass spectrometric data deposit in ProteomeXchange/PRIDE. We thank excellent contributions from the micro-PET core facility of the University of Navarra (M. Collantes and M. Ecay) and the Morphology Core Facility [Universidad de Navarra, Centro de Investigación Médica Aplicada (CIMA)] for the support with histological studies. We gratefully acknowledge G.K. for providing the GLUT1 floxed mouse line. We thank Amanda Sierra for protocol sharing and support. Figures 2A, 3E, 4N, 6E, 7C, and 8D were created with BioRender.com. **Funding:** This work was financially supported by grants SAF2017-87619-P and PID2021-128737NB-I00 funded by MCIN/AEI/10.13039/501100011033 and by "ERDF A way of making Europe," and NARSAD Young Investigator grant from the Brain & Behavior Research Foundation (grant number 28177). This work was also supported by a grant from CIBERDEM (ISCIII, Spain) to M.P.V. and Á.M.V. C.G.A. is supported by an FPU (Formación de Profesorado Universitario) fellowship from the Spanish Ministry of Universities (FPU18/01458). **Author contributions:** Conceptualization: M.S. and C.G.A.; Methodology: M.S., C.G.A., P.S.M., J.F.-I., M.Á.P., C.O.-d.-S., E.P., G.K., M.E.-H., J.E.O., and P.V.V. Software: M.A., P.S.M., C.O.-d.-S., and M.E.-H. Validation: M.S., C.G.A., P.S.M., M.J.R., M.Á.P., M.E.-H., and P.V.V. Formal analysis: M.S., C.G.A., M.A., A.d.l.C., J.F.-I., M.Á.P., E.S., M.E.-H., P.V.V. Investigation: C.G.A., M.S., A.d.l.C., P.S.M., Á.M.V., J.F.-I., N.H.-M., M.Á.P., E.P., C.E., A.U., E.S., J.E.O., and P.V.V. Resources: M.S., P.S.M., Á.M.V., M.J.R., M.Á.P., E.P., C.E., A.U., E.S., J.E.O., P.V.V., and J.C.B. Data curation: M.S., P.S.M., M.E.-H., and P.V.V. Writing (original draft): M.S., C.G.A., P.S.M., and P.V.V. Writing (review and editing): C.G.A., M.S., M.A., P.S.M., J.F.-I., M.J.R., M.Á.P., E.P., M.E.-H., and J.C.B. Visualization: M.S., C.G.A., M.A., A.d.l.C., P.S.M., Á.M.V., M.J.R., M.Á.P., and P.V.V. Supervision: M.S., C.O.-d.-S., and J.C.B. Project administration: M.S. Funding acquisition: M.S. and Á.M.V. **Competing interests:** The authors declare that they have no competing interests. **Data and materials availability:** Proteomics data have been deposited at ProteomeXchange/jPOST and are publicly available with the identifier PXD035376 for ProteomeXchange and JPST001793 for jPOST (https://repository.jpostdb.org/entry/JPST001793). Original Western blot images have been deposited at Mendeley and are publicly available (DOI: 10.17632/zdc9tmktjp.1). All raw data have been deposited at Zenodo and are publicly available (10.5281/zenodo.12740848). The code used to build a weighted protein coexpression signed network is the WGCNA package (https://cran.r-project.org/web/packages/WGCNA/index.html) in R (www.r-project.org). All data needed to evaluate the conclusions in the paper are present in the paper and/or the Supplementary Materials.

Submitted 7 March 2024
Accepted 13 September 2024
Published 18 October 2024
10.1126/sciadv.adp1115